



**HAL**  
open science

## A speciation model linking the fate of carbon and hydrogen during coremagma ocean equilibration

Fabrice Gaillard, Valérie Malavergne, Mohamed Ali Bouhifd, Gregory Rogerie

### ► To cite this version:

Fabrice Gaillard, Valérie Malavergne, Mohamed Ali Bouhifd, Gregory Rogerie. A speciation model linking the fate of carbon and hydrogen during coremagma ocean equilibration. *Earth and Planetary Science Letters*, 2022, 577, pp.117266. 10.1016/j.epsl.2021.117266 . insu-03419023

**HAL Id: insu-03419023**

**<https://insu.hal.science/insu-03419023v1>**

Submitted on 8 Nov 2021

**HAL** is a multi-disciplinary open access archive for the deposit and dissemination of scientific research documents, whether they are published or not. The documents may come from teaching and research institutions in France or abroad, or from public or private research centers.

L'archive ouverte pluridisciplinaire **HAL**, est destinée au dépôt et à la diffusion de documents scientifiques de niveau recherche, publiés ou non, émanant des établissements d'enseignement et de recherche français ou étrangers, des laboratoires publics ou privés.

# 1 **A speciation model linking the fate of carbon and hydrogen during core –** 2 **magma ocean equilibration**

3

4 Fabrice Gaillard<sup>1</sup>, Valérie Malavergne<sup>2</sup>, Mohamed Ali Bouhifd<sup>3</sup>, Gregory Rogerie<sup>1</sup>

5

6 1- Université d'Orléans, CNRS, BRGM, ISTO, UMR 7327, F-45071, Orléans, France.

7 2- Université Paris Est-Marne La Vallée, Laboratoire des Géomatériaux et Environnement,  
8 Champs-sur-Marne, 77454 Cedex, France.

9 3- Laboratoire Magmas et Volcans, Université Clermont Auvergne, CNRS, IRD, OPGC, F-  
10 63000 Clermont-Ferrand, France.

11

12

## 13 **Abstract.**

14 The core – mantle differentiation in the magma ocean constitutes a major planetary event that  
15 involved two elements that are essential to life: carbon (C) and hydrogen (H). These two  
16 elements are conventionally classified as volatiles (ie. atmophile), but they can also evolve into  
17 being siderophile and lithophile at the extreme conditions found in planetary magma oceans.  
18 We report here a model for H and C species dissolved in silicate melts in equilibrium with iron-  
19 rich alloys under variable pressure, temperature and redox conditions. This speciation model is  
20 able to reconcile and reproduce a large body of experimental data on metal-silicate partitioning  
21 for H and C at carbon-saturation and in C-undersaturated systems. At low pressure, we conclude  
22 that the prevailing species in a silicate magma ocean are CO<sub>2</sub>, CO, H<sub>2</sub>O, H<sub>2</sub>, whereas CH<sub>4</sub>  
23 appears to dominate at high pressure. These speciation changes explain recent experimental  
24 observations that (i) C evolves from being strongly siderophile at low pressure to moderately

25 siderophile at high pressure, and (ii) H is not siderophile at low pressure but becomes  
26 increasingly so as pressure rises. Moreover, it shows that H becomes increasingly siderophile  
27 as the total H content of the silicate melt and C-activity are lowered. Despite it offers a  
28 promising reconciliation of a large set of experimental and molecular dynamics observations,  
29 this model still suffers from large uncertainties when extrapolated to high pressure. In  
30 particular, endmember and mixing properties in both the silicate melt and the molten metal  
31 must be independently deciphered.

32 The enhanced CH<sub>4</sub> stability in the silicate melt at high pressure couples the fate of C and H in  
33 deep magma oceans. In such cases, the solubility of C in the basal ocean depends on the H-  
34 content and is higher than C-solubility at low pressure. This implies an increase in C activity as  
35 the ascending convective cells of the magma ocean, which may cause C saturation as graphite  
36 or diamond unless Fe-metal droplets, having a great C-solubility, are present in the shallow  
37 magma ocean. Under certain conditions, enhanced siderophile behaviour for H can lead via a  
38 runaway process to the desiccation of the magma ocean.

39

40

41

## 42 **1. Introduction**

43 Terrestrial planets evolved through early magma ocean stages (Rubie et al. 2015). These magma  
44 oceans were highly diverse on planetesimals, planetary embryos, and planets, implying  
45 increasingly extreme temperature and pressure conditions (*eg.* Li et al., 2016; Siebert et al.,  
46 2012). These molten stages are believed to provide an essential medium permitting planetary  
47 differentiation into a core, mantle, early crust and early atmosphere. Magma ocean is a general  
48 term embodying a silicate melt, with a varying fraction of silicate crystals, possibly coexisting

49 with molten metallic Fe-rich alloys, sulfide, carbide, graphite, diamond and a fluid phase. A  
50 major part of our understanding of the magma ocean stages on Earth is deduced from the  
51 interpretation of mantle depletion in variably siderophile elements through metal –silicate  
52 equilibria (*e.g.* Wade and Wood, 2005; Siebert et al., 2012; Rubie et al., 2015; Badro et al.,  
53 2015). The cause of mantle depletion of moderately siderophile elements with respect to  
54 chondritic abundances is generally attributed to the sequestration of the depleted elements into  
55 the core. Given the growing interest in the conditions defining habitable worlds, the distribution  
56 of C and H, two life-essential elements, during the magma ocean stage has been thrust into the  
57 scientific limelight (Okuchi, 1996; Hirschmann, 2012a; Sarafian et al., 2014; Li et al., 2016;  
58 Clesi et al., 2018; Malavergne et al., 2019; Greenwood et al., 2018; Grewal et al., 2019; Fischer  
59 et al., 2020; Li et al., 2020; Tagawa et al., 2021; Gaillard et al., 2021). At the pressure (P) –  
60 temperature (T) – redox conditions (oxygen fugacity  $f_{O_2}$ ) of modern magmatic and volcanic  
61 settings, C and H are considered as volatile elements or atmophile, ie. with a great affinity for  
62 the vapor phase (Iacono-Marziano et al., 2012). However, during the magma ocean stages,  
63 conditions were strongly reduced, and involved variable P-T conditions (1-60 GPa, 1500-  
64 4000°C), implying that some supposedly volatile elements could become magmatophile or  
65 siderophile and change the metal-silicate systematics (Ohtani et al., 2005; Hirschmann, 2012a;  
66 Gaillard et al., 2021). Wood et al. (2013), in their review paper, used a combination of  
67 thermodynamics, experimental data and isotopic constraints to predict a significant affinity of  
68 C for the metallic phase (of about 1 wt%) during metal-silicate equilibria taking place during  
69 the magma ocean stage. Okuchi (1996) reported experiments at high P and high-T (7 GPa,  
70 1200-1500°C) revealing that H could be moderately siderophile. Capturing the behaviour of  
71 these elements during core formation is therefore not only important for deciphering the origin  
72 of a 5 to 10% density deficit in the Earth’s core, but also because it may be a major stage in the  
73 construction of habitable worlds.

74 Recently, several research groups have produced experiments tackling the behaviour of C  
75 during metal silicate equilibration (eg. Wetzel et al., 2013; Dasgupta et al., 2013; Kadik et al.,  
76 2014; Stanley et al., 2014 ; Malavergne et al. 2019 ; Kuwahara et al. 2019; Fischer et al., 2020).  
77 These studies have reported equilibrium partitioning of C between molten Fe-rich metal and  
78 silicate melt at variable P, T,  $fO_2$  and water (or H) contents. All these parameters affect the  
79 partitioning of C between metal and silicate. Using empirical linear relationships between the  
80 different variables (Eguchi and Dasgupta, 2018; Malavergne et al., 2019; Fisher et al., 2020),  
81 the dependencies of C partitioning on  $fO_2$ , T, P, water content and the amount of non-bridging  
82 oxygen per tetrahedron (NBO/T) have been fitted (NBO/T is an empirical parameter long  
83 known to control the solubility of carbon dioxide in molten silicates, eg. Iacono-Marziano et  
84 al., 2012). Most of these experimental studies also involved H (ie. often reported as water) and  
85 determined the H-content in the silicate melts, but so far, only three studies measured the  
86 partitioning of H between metal and silicate melts (Okuchi, 1996; Clesi et al., 2018; Malavergne  
87 et al., 2019) to 21 GPa, and recently, Tagawa et al (2021) indirectly estimated  $D^H$  at 30-60 GPa  
88 3100-4600 K (using the phase proportions and the cell volume of  $FeH_x$  et  $\epsilon$ - $FeOOH$  to get the  
89 H content in metals). These studies reported significant effects of P, T and  $fO_2$  on H metal-  
90 silicate partitioning that are consistent with molecular dynamics calculations at extreme P and  
91 T (Zhang and Yin, 2012; Li et al. 2020, Yuan and Steinle-Neumann, 2020). Finally, empirical  
92 relationships have also been established to predict the molten metal – silicate liquid partitioning  
93 of H (Clesi et al., 2018; Malavergne et al., 2019; Tagawa et al 2021).

94 All these linear empirical models are phenomenological laws that do not consider the C-O-H  
95 chemical speciation in the silicate melts and their dependence on P, T and  $fO_2$ , which control  
96 H and C partition coefficients. These empirical approaches are interesting because they can  
97 provide input for a timely discussion generalizing and interpolating the experimental data points  
98 (eg. Fischer et al., 2020). However, equilibria related to the partition coefficient of an element

99 involving several species is, in principle, not constant and cannot be solved using a linear  
100 relationship. In our case for example, partitioning of C involves at least three species in the  
101 silicate melt: CO, CO<sub>2</sub>, CH<sub>4</sub> (Armstrong et al., 2015), while the partitioning of H implies at least  
102 OH, H<sub>2</sub>O, H<sub>2</sub> and CH<sub>4</sub> as dissolved species in the silicate melts. Here, we establish a  
103 thermochemical framework defining and linking the speciation of C and H in the silicate melt  
104 at the extreme conditions of the magma ocean. Even if this formalism is simple, it allows us to  
105 calculate with a unique formalism, the partitioning of both C and H between molten metal and  
106 silicate liquid, including C-undersaturated cases. This formalism shows that the current dataset,  
107 produced in various laboratories and covering a vast P-T-fO<sub>2</sub>-volatile activity conditions, is  
108 consistent. However, high pressure solubility C-O-H data in metals and silicate melts, as well  
109 as some key thermodynamic parameters (such as compressibility) are missing rendering the  
110 extrapolation of this model to pressure greater than 30 GPa more challenging and uncertain.  
111 This approach paves the way for a broadened model to cover larger chemical systems (eg. to  
112 include other volatile elements such as O, S, and N and a vapour phase).

113

## 114 **2. The database**

115 Table 1 summarizes the 161 experiments used for the present thermochemical modelling. These  
116 experimental studies were conducted in the pressure range 1-21 GPa, in the temperature interval  
117 1350 -2327 °C and with a fO<sub>2</sub> varying from -5.3 to +1.8 relative to the Iron-Wüstite (IW) redox  
118 buffer. The entire database (but Clesi et al, 2018) gives the C and H content of silicate melts at  
119 C-saturation. We have selected the experimental studies in which both H and C contents in the  
120 silicate melt were determined, thus the recent high-P work by Fischer et al. (2020), Fichtner et  
121 al. (2021) and Tagawa et al (2021) could not be used here (see the 2-next paragraphs). Clesi et  
122 al. (2018) did not measure the C-content in the silicate melts but C-contents in silicate melts at  
123 C-saturation under the P-T-fO<sub>2</sub>-fH<sub>2</sub>O conditions of their experiments is mostly provided by

124 other studies. The range of H-content in silicate melts (Table 1), converted into H<sub>2</sub>O, is 0.009  
125 (Armstrong et al. 2015) to 5 wt% (Kadik et al. 2014), which covers the expected conditions for  
126 any magma ocean. All experiments are C-saturated and provide the C-content of metals, but  
127 only two papers provide H concentrations in metals (20 experiments from Malavergne et al.,  
128 2019 and Clesi et al, 2018). Some experiments were excluded because the metal compositions  
129 were too rich in S (cut >1%) or Ni (cut at >10%), but this concerns only a four experiments in  
130 Li et al. (2015).

131

132 *Table 1. Summary of the experimental studies considered. All experiments are C-saturated.*

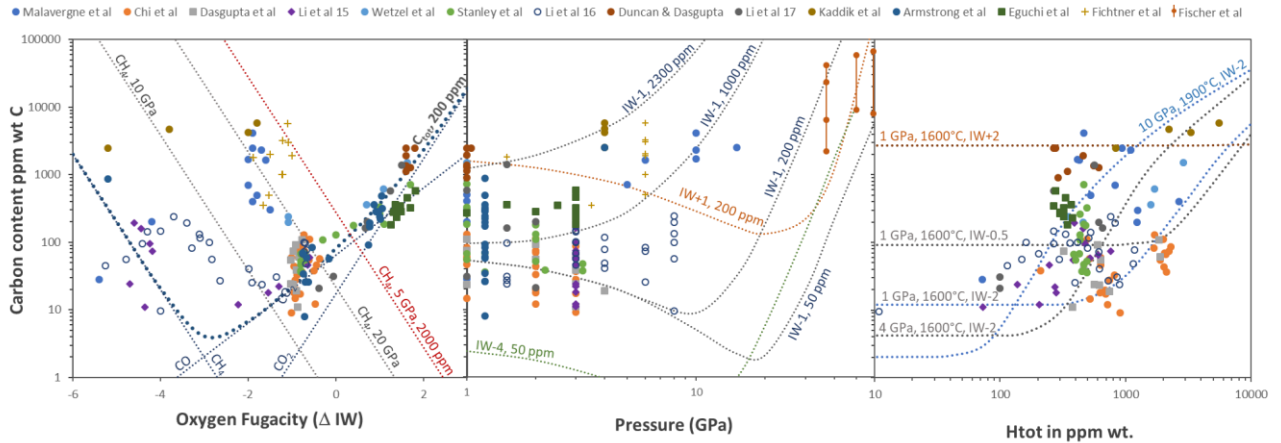
Authors	P range (GPa)	T (°C)	range	fO <sub>2</sub> range	SILICATE MELT		METAL	
					C ppm	H ppm	C wt%	H ppm
Malavergne et al. 2019	1-15	1400-2300		-5.4 : -1.6	28-4100	277-1243	3.4-7	13-236
Clesi et al. 2018	5-21	1747-2427		-3.8 : -0.7	nd	402-1234	4.2-7.5	59-254
Eguchi & Dasgupta 2017	1-3	1425-1550		0.3 : 1.3	171 - 579	267-378	N.A.	N.A.
Li et al. 2017	1-2	1400-1550		-0.4 : 1.5	21 - 1388	100-656	N.A.	N.A.
Duncan et al., 2017	1	1600		1.6 : 1.8	900-2455	291-556	N.A.	N.A.
Li et al., 2016	1.5-8	1600-2200		-5.3 : -0.7	10-241	11-1172	3.03-5.7	N.A.
Stanley et al., 2014	1-3	1340-1617		-0.8 : 1.7	36-716	384-489	N.A.	N.A.
Wetzel et al., 2013	0.85 – 1	1500-1530		-1.1 : 1.6	199-1503	345-1698	7.6-8.3	N.A.
Armstrong et al., 2015*	1.2	1400		-1 : 1.5	8 - 864	10-1188*	6.2-7.7	N.A.
Li et al., 2015	3	1600		-4.7: -0.6	11 - 192	73 - 760	3.4-5.9	N.A.
Chi et al., 2014	1-3	1500-1800		-1 : -0.4	9-129	210-2284	4.9-7.2	N.A.
Dasgupta et al., 2013	1-4	1600-2000		-1 : -0.8	11-93	321-1890	4.8-8.5	N.A.
Kadik et al. 2014	4	1550		-1.8: -3.4	4200-5800	2200-5500	N.A.	N.A.

134 \* Only water (OH bonds), measured by FTIR, are given in this paper.

135 Figure 1 reports the C-content in silicate melts at C-saturation vs. fO<sub>2</sub>, P and total H contents in  
136 the melts. For the experiments at fO<sub>2</sub><IW, these silicate melts are saturated in metal Fe  
137 containing 5-7 wt% C. Considering these metal-saturated experiments, we distinguished two  
138 groups of datapoints: a group with ca. <200 ppm C (low pressure, 1-5 GPa and low H content)  
139 and another one with C-content > 200 ppm (high pressure and/or high H-content). Such a large  
140 range of C contents dissolved in silicate melts at graphite-saturation (8-5800 ppm, Table 1,



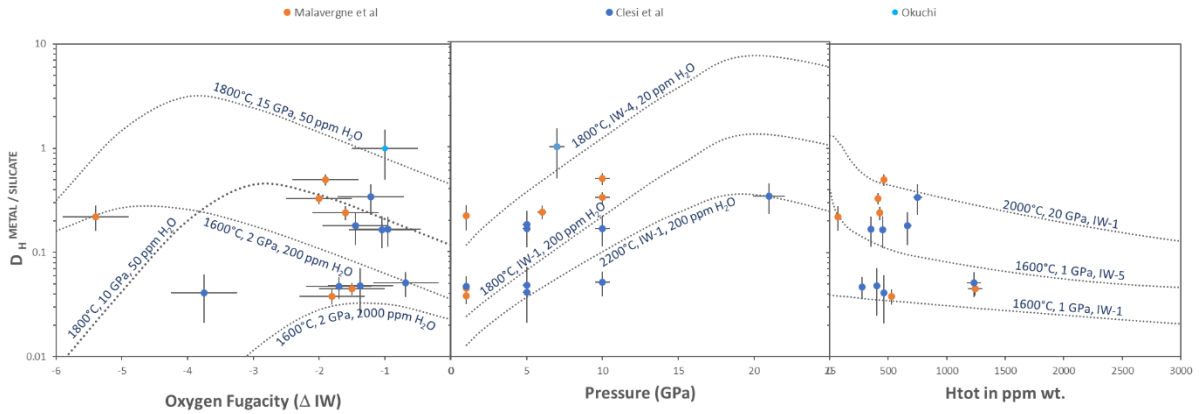
141 Figure 1) may then reflect a range of C-speciation ( $\text{CO}_2$ , CO and  $\text{CH}_4$ , eg. Armstrong et al.,  
142 2015). But this large range has also cast doubt on the validity of some data. Recently, Fichtner  
143 et al (2021) argued that most of the data in table 1 and figure 1 are flawed due to a poor  
144 attainment of equilibrium. The point raised is that adding C as carbonate in the silicate starting  
145 material is a necessity to enhance equilibration rates since graphite-melt reactions are otherwise  
146 too sluggish. The datapoints of Fichtner et al. (2021) are indeed higher than most of the database  
147 (Figure 1a,1b) leading to the suspicion of unequilibrated C-contents in the silicate melts of most  
148 experimental data of table 1. In details, however, Fitchner et al. (2021) data indicates a range  
149 of C-content that is comparable to the studies of Malavergne et al. (2019) and Kadik et al.  
150 (2014) (see next paragraph). These three studies reported experiments that lasted ca. 10 minutes  
151 to 1 hour, whereas most other experiments of table 1, which are suspected of problem of  
152 equilibration, lasted a couple of hours: equilibration issues seem unlikely. It is also hardly  
153 conceivable that the C content of the glass would be far below equilibrium (and very low, eg  
154  $\ll 200$  ppm C), whereas the metal blobs spread in these glasses do show a high range of C-  
155 content (5-7 wt% C) that are consistent with C-saturation: if isolated metal blobs are C-  
156 saturated, the surrounding glass, connecting graphite to metal blobs, must also be equilibrated.  
157 Here, we consider that deviation of equilibration is a possibility for some data, but the  
158 generalisation of such a deviation is not justified by the existing experimental constraints taken  
159 as a whole: the range of C-content in figure 1 must reflect speciation effects.



160

161 *Figure 1: C content at C-saturation versus  $f_{O_2}$ ,  $P$  and  $H$ -content in the silicate melts. The*  
 162 *database of Table 1 is shown here. The lines show calculations using the C-O-H speciation*  
 163 *model for a range of  $P$ - $T$ - $H$ - $f_{O_2}$  conditions that are representative of the conditions covered by*  
 164 *the database. The data of Fichtner et al (2021) and Fischer et al (2020) are also shown though*  
 165 *they have not been used to calibrate the speciation model. The data of Fichtner et al (2021) and*  
 166 *Fischer et al (2020) can respectively be explained using the speciation model with ca. 1000-*  
 167 *2000 ppm and ca. 50-200 ppm  $H_2O$  respectively.*

168 As noticed before, the datapoints of Kadik et al. (2014) and some of Malavergne et al (2019)  
 169 display both high C and high H contents (dissolved in the melt). This may reflect a higher  
 170 proportion of  $CH_4$ . Regrettably, this assessment cannot be verified with the data of Fichtner et  
 171 al (2021) since the H content of their samples is unknown. Fichtner et al. (2021) stated that their  
 172 samples must be  $< 5000$  ppm  $H_2O$ , which remains elevated, and they reported RAMAN spectra  
 173 indicating dissolved  $CH_4$ . Elevated C content reported in Fichtner et al (2021) may then also  
 174 reflect a significant amount of  $CH_4$  in the glass. Another study, Fischer et al (2020), also  
 175 reported high amounts of dissolved C, whereas the H contents of the glass are unknown. These  
 176 data were collected at very high  $P$  and  $T$  (Figure 1b). Noteworthy, the RAMAN spectra of these  
 177 samples revealed that  $CH_4$  is the dominant dissolved form of C.



178

179 *Figure 2: H metal-silicate partitioning versus  $f_{O_2}$ ,  $P$  and  $H$ -content in the silicate melts. We*  
 180 *show here the data of Clesi et al (2018), Malavergne et al (2019) and Okuchi (1996). The lines*  
 181 *show calculations using the C-O-H speciation model for a range of P-T-H- $f_{O_2}$  conditions that*  
 182 *are representative of the conditions covered by the database. The high-pressure ( $P > 30$  GPa)*  
 183 *MD data of Li et al (2020) and that experimental data of Tagawa et al (2021) are not shown*  
 184 *for sake of simplicity and because these were not used to calibrate our model.*

185 The 15 experimental H-partitioning data are shown in figure 2. Clesi et al (2018) and  
 186 Malavergne et al (2019) have reported metal-silicate partitioning data at C-saturation in the  
 187 pressure range 1-21 GPa, whereas Okuchi (1996) reported C-free data at 7 GPa. We can  
 188 distinguish C-saturated data being in the range  $D_H \sim 0.03-0.6$ , whereas C-free data are in the  
 189 range  $D_H \sim 1$  or slightly higher. Using molecular dynamics calculations, Li et al (2020)  
 190 corroborated that H is siderophile in C-free conditions (ie.  $D_H > 1$ ) and they showed that  $D_H$   
 191 increases with increasing  $P$  (to 20-135 GPa). The recent study of Tagawa et al (2021) also  
 192 confirms this result, though, we recall that the H-content in their Fe-alloys was indirectly  
 193 estimated. This positive  $P$  dependence has also been reported in C-saturated conditions (Clesi  
 194 et al., 2018; Malavergne et al., 2019) in the range 1-21 GPa (Figure 2).

195 To conclude on this brief review of available data on C and H metal-silicate partitioning, we  
 196 see that the partitioning systematics of both elements are linked: C partitioning (or C-content at

197 C-saturation) depends on H-contents, and H-partitioning is different in C-free and C-saturated  
 198 conditions. In both cases, a significant effect of P has been noticed, rendering H more  
 199 siderophile and C less siderophile. Below we present a simple thermodynamic framework that  
 200 relates C and H speciation in silicate melts to changes in metal-silicate partition coefficients in  
 201 P-T-fO<sub>2</sub>-fH<sub>2</sub>O parameter space.

202

### 203 3. Data Reduction

204 Each of the treated equilibria follows a law of mass action involving the constant of the reaction  
 205 (K), in which the P and T dependences of the reaction's Gibbs free energy ( $\Delta G_r$ ) are  
 206 approximated by the relationship:

$$207 \log K = -\frac{\Delta G_r}{RT} = \frac{A}{T} + B + C \times \frac{P}{T} \quad (1)$$

208 A, B and C are respectively related to the changes in enthalpy, entropy and volume associated  
 209 with the reaction. Accordingly, in C-saturated charges, the C-content in metal ( $C^{\text{METAL}}$ ) is  
 210 defined as follows:

$$211 C^{\text{GRAPHITE}} = C^{\text{METAL}} \quad \text{with} \quad \log K_2 = \log C^{\text{METAL}} + \log \gamma_C^{\text{METAL}} + \frac{A_2}{T} + B_2 + C_2 \times \frac{P}{T} \quad (2)$$

212 Here,  $\gamma_C^{\text{METAL}}$  stands for the activity coefficient of C in the Fe-metal (see supplementary  
 213 section). At this stage, we consider  $\gamma_C^{\text{METAL}}$  to be P independent.

214 In the silicate melts of the C-O-H system, the total C-content is considered as being the sum of  
 215 three species: CO<sub>2</sub>, CO, and CH<sub>4</sub>. Expressed in mass fraction, this yields:

$$216 C^{\text{tot}} = \frac{CO_2}{44} \times 12 + \frac{CO}{28} \times 12 + \frac{CH_4}{16} \times 12 \quad (3)$$

217 The total H content in the silicate melts is considered as being the sum of three species: H<sub>2</sub>O,  
 218 H<sub>2</sub>, CH<sub>4</sub>. Expressed as a mass fraction, this yields:

$$219 \quad H^{tot} = \frac{H_2O}{18} \times 2 + \frac{H_2}{2} \times 2 + \frac{CH_4}{16} \times 4 \quad (4)$$

220 In most of the experimental conditions (Table 1), all H<sub>2</sub>O is dissolved in the silicate melt, mostly  
 221 as OH (Newcombe et al., 2017), but we computed these OH as H<sub>2</sub>O equivalent (eg. Iacono-  
 222 Marziano et al., 2012). This C-O-H speciation appears to be consistent with current state-of-  
 223 the-art surveys (eg. Kadik et al., 2014; Armstrong et al., 2015, Malavergne et al., 2019; Dalou  
 224 et al., 2019; Fischer et al. 2020). However, we admit that, in view of the limited number of  
 225 studies on HP-HT speciation of C-O-H species in silicate melts, additional species may need to  
 226 be considered in future models (eg. FeCO, CH<sub>x</sub> or CO<sub>x</sub> species; see Wetzel et al., 2013 ; Ardia  
 227 et al., 2014 ; Kadik et al., 2014; Dalou et al., 2019; Solomatova et al., 2019).

228 The solubility of CO<sub>2</sub>, CO and CH<sub>4</sub> are defined at C-saturation as:



232 We considered CO<sub>2</sub> as an anionic species in the silicate (CO<sub>3</sub>)<sup>2-</sup>, implying that its solubility  
 233 depends on oxygen O<sup>2-</sup> activities in the melt in addition to fO<sub>2</sub>. Iacono-Marziano et al. (2012)  
 234 did use the NBO/T parameter as a proxy of O<sup>2-</sup> activity to model carbonate solubility in mafic  
 235 melts. This approach has also been considered in recent models on the C content at graphite  
 236 saturation (Li et al. 2017). Accordingly, equilibria (5) and (6) are respectively modelled as:

$$237 \quad \log K_5 = \log CO_2 + \frac{A_5}{T} + B_5 + C_5 \times \frac{P}{T} - \log fO_2 + D_5 \times \frac{nbo}{t} \quad (8)$$

$$238 \quad \log K_6 = \log CO + \frac{A_6}{T} + B_6 + C_6 \times \frac{P}{T} - 0.5 \times \log fO_2 \quad (9)$$

239 Equilibria (7) is described as follows:

$$240 \quad \log K_7 = \log CH_4 + \frac{A_7}{T} + B_7 + C_7 \times \frac{P}{T} + \log fO_2 + 2 \times \log H_2O \quad (10)$$

241 In equations (8-10), CO<sub>2</sub>, CO, CH<sub>4</sub> and H<sub>2</sub>O refer to the activity of these species in the silicate  
242 melt. The activity of CO and CH<sub>4</sub> is equal to their mole fraction in the melt (assumed given the  
243 low concentrations and the absence of proof of more complicated behaviour). The activity of  
244 CO<sub>2</sub> depends on NBO, and that of H<sub>2</sub>O in silicate melts has long been known to be proportional  
245 to the square of the H<sub>2</sub>O concentration (Newcombe et al., 2017 and references therein).  
246 Accordingly, in all equilibria involving H<sub>2</sub>O, its activity was computed as the square of the H<sub>2</sub>O  
247 melt content.

248 The total C content in silicate melts at C-saturation has been parameterized by merging eq. (3)  
249 and eqs. (8-9-10). Since the activity of C,  $a_C$ , is 1,  $\log a_C$  is null and is therefore absent in  
250 equations (8) to (10), but C undersaturation in the metallic phase can be considered by adding  
251 the term  $-\log a_C$  to equations (8-10).

252 The H content in silicate melts is computed by merging eq. (4), eq. (7) and the following  
253 equilibria:



255 The equilibrium constant for eq. (11) is written as:

$$256 \quad \log K_{11} = \log H_2O - \log H_2 + \frac{A_{11}}{T} + B_{11} + C_{11} \times \frac{P}{T} - 0.5 \times \log fO_2 \quad (12)$$

257 H<sub>2</sub> refers here to the mole fraction of H<sub>2</sub> dissolved in the silicate melt (Hirschmann, 2012b).

258 The partitioning of H between silicate melt and metal has been calculated as:



260  $\log K_{13} = 4 \times \log H + \log CO - \log CH_4 + \frac{A_{13}}{T} + B_{13} + C_{13} \times \frac{P}{T} - 0.5 \times \log fO_2$  (14)

261 Considering other stoichiometry (see Clesi et al., 2018) such as:



263 these are all equivalent, since all the species involved are linked by equilibria (5-6-7-11) and  
 264 by the mass balance constraints (eqs. 3-4). This means that the partition coefficient of H can be  
 265 computed as:

266  $D_H^{metal/silicate} = \frac{H^{metal}}{H^{silicate}} = \frac{H^{metal}}{\frac{CH_4^{silicate}}{16} \times 4 + \frac{H_2^{silicate}}{2} \times 2 + \frac{H_2O^{silicate}}{18} \times 2}$  (16)

267 All thermodynamic constants involved in equations (8-10 and 14) are simultaneously adjusted  
 268 in order to reproduce the P-T-fO<sub>2</sub>-H<sub>2</sub>O dependences of the C-content in the silicate melt at C-  
 269 saturation and the metal silicate partitioning of H. In practice, we minimized the following sum:

270  $S_{optimal} = f(H^{SILICATE}) + f(C^{SILICATE}) + f(H^{METAL}) + f(D_H^{METAL})$

271 with  $f(H^{SILICATE}) = \frac{|H_{measured}^{tot} - H_{calculated}^{tot}|}{\partial_{H^{tot}}}$ ,  $f(C^{SILICATE}) = \frac{|C_{measured}^{tot} - C_{calculated}^{tot}|}{\partial_{C^{tot}}}$ ,

272  $f(H^{METAL}) = \frac{|H_{measured}^{METAL} - H_{calculated}^{METAL}|}{\partial_{H^{METAL}}}$  and  $f(D_H^{METAL}) = \frac{|D_{H_{measured}^{METAL}} - D_{H_{calculated}^{METAL}}|}{\partial_{D_H^{METAL}}}$

273  $\delta$  refers to the analytical error on the measured values as reported in the original study (we  
 274 considered  $2\sigma$ ). This specific effort was justified by the fact that reported errors greatly vary  
 275 from a study to another and from a sample to another.

276

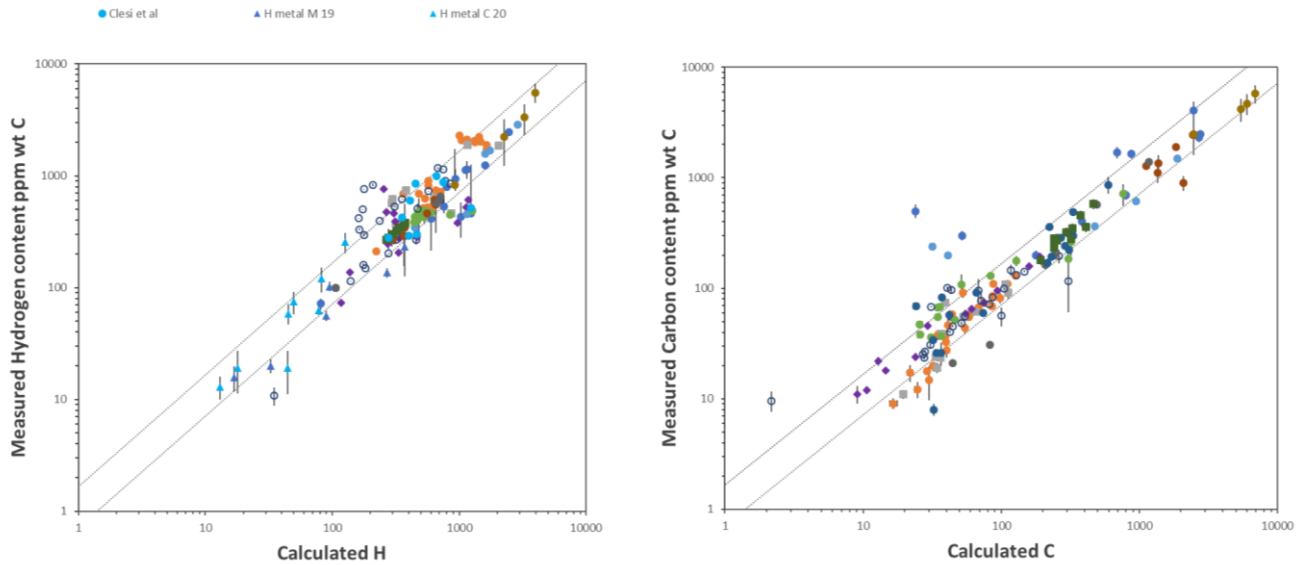
## 277 **4. Predicting partitioning data in the parameter space**

### 278 4.1. Accuracy

279 In a simultaneous fitting process, all thermodynamic constants  $A_i$ ,  $B_i$ ,  $C_i$  appearing in equations  
280 (2, 8, 9, 10, 12, 14) have been parameterized in order to reproduce the P-T- $fO_2$  dependences of  
281 the C and H contents in a silicate melt and metals at C-saturation. The list of parameters is given  
282 in supplementary table S1. The results of the fit are given in figure 3 in terms of H and C-  
283 contents in a silicate melt at C-saturation. Recalculated data for H- and C-contents at C-  
284 saturation deviate on average by less than 33 % from the experimentally determined values (see  
285 Fig. 3; see also figure S1). Outlier datapoints concern a few experiments that conflict with the  
286 rest of the database, whereas P-T-H- $fO_2$ -conditions are otherwise similar.

287 Uncertainties assessment on the  $A_i$ ,  $B_i$ ,  $C_i$  parameters adjusted using such non-linear multi-  
288 parameter fitting has no unique solution. We performed sensitivity tests on each adjusted  
289 parameter. This consists in varying each fitted parameter in order to probe its effect on the  
290 function *Soptim* (eq. 17, see figure S2). The upper and lower bounds for the  $A_i$ ,  $B_i$ ,  $C_i$  parameters  
291 were computed to match an increase of the *Soptim* function by 30% maximum (ie. an increase  
292 of the misfit by 30%, see figures S2). This 30% value corresponds to the mean accuracy of our  
293 model (see Fig. S1, where  $1\sigma=15\%$ ). Quoted uncertainties are reported in table S1. Given the  
294 reported experimental uncertainties (in P, T,  $fO_2$ , H and C-contents) and the possible issue of  
295 calibration between different studies, we consider that the speciation model described here can  
296 reproduce the observed saturation and partitioning data reasonably well. The C and H contents  
297 and their uncertainties (a comprehensive error propagation formalism has been made available)  
298 can be calculated using our model in an online application [http://calcul-isto.cnrs-](http://calcul-isto.cnrs-orleans.fr/apps/silicate_melt/)  
299 [orleans.fr/apps/silicate\\_melt/](http://calcul-isto.cnrs-orleans.fr/apps/silicate_melt/)). Uncertainties in calculated C and H contents in silicate melts  
300 range from ca. 10% at pressure of 1 GPa-1600°C, 15-25 % at 10 GPa-1800°C, 20-50% at 30-  
301 2000°C GPa and 90-110% at 50 GPa, 3000°C. Uncertainties in calculated C and H contents in  
302 metal and  $D_C$  and  $D_H$  are propagated on the web-application through the various equations listed  
303 on section 3.





305

306 *Figure 3: Observed vs predicted Carbon Content at C-saturation (CCCS) and H content in*  
 307 *silicate melts and metals. The legend is similar to that used in figure 1 and the additional data*  
 308 *are specified just above the left figure; these include the H-data of Clesi et al (2018) and*  
 309 *Malavergne et al (2019). The 33% misfit lines are reported here. Outlier datapoints concern a*  
 310 *few experiments that conflict with the rest of the database (P-T-H-fO<sub>2</sub>-conditions being*  
 311 *otherwise similar).*

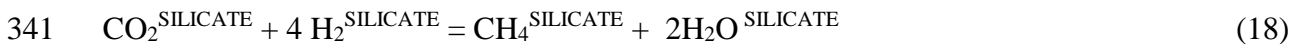
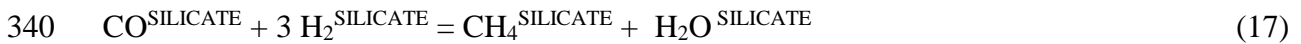
312

#### 313 4.2. C-speciation in P-T-fO<sub>2</sub> parameter space.

314 Figure 1 illustrates the speciation methodology used to capture the C-content in silicate melt at  
 315 C-saturation in metal. It shows the silicate melt C-contents at C-saturation vs. fO<sub>2</sub>, vs. P and vs.  
 316 total H content in the silicate melts taken from the entire experimental database; it also  
 317 superimposes the calculated C-speciation at various fO<sub>2</sub>-P-T-H<sub>2</sub>O conditions. In figure 1a, the  
 318 thick dotted blue line shows the C<sub>tot</sub> (the sum of C as CO<sub>2</sub>+CO+CH<sub>4</sub>) at 2 GPa, 1500°C and for  
 319 a H<sub>2</sub>O content in the melt of 200 ppm. The fO<sub>2</sub> dependences of the fraction of C as CO<sub>2</sub>, CO  
 320 and CH<sub>4</sub> are shown with the thin dotted blue straight lines. We clearly see CO<sub>2</sub> being the

321 dominant form of C at high  $fO_2$ , CO at intermediate  $fO_2$  and  $CH_4$  at the lowest  $fO_2$ . The  
 322 crossover  $CO_2$ -CO occurs at an  $fO_2$  of about  $IW+1$ , as observed in specific experimental  
 323 surveys (eg. Armstrong et al., 2015). The crossover CO- $CH_4$  occurs at ca.  $IW-3$ , but changing  
 324 P or the  $H_2O$  content strongly modify this  $fO_2$  values. For example, increasing P significantly  
 325 increases the threshold  $fO_2$ , which becomes ca.  $IW-0.5$  at 20 GPa. This P effect explains some  
 326 of the Malavergne et al (2019) data. Increasing  $H_2O$  content also greatly increases the amount  
 327 of  $CH_4$ , which can become the dominant form of dissolved C at 5 GPa- $IW$ . This explains well  
 328 the data of Kadik et al. (2014) that has so far been ignored in existing modelling (ie. Li et al.,  
 329 2017; Eguchi et al., 2018; Fischer et al., 2020).

330 Figure 1b shows the P effect on C content at C-saturation. Calculated values bracket well the  
 331 experimental data when considering a representative range of P-T- $fO_2$  conditions. These  
 332 calculations also reveal two opposite trends. Moderately hydrated melts ( $\leq 200$  ppm  $H_2O$ ) show  
 333 C-solubility that decreases with increasing P (to ca. 10-20 GPa), whereas hydrated melts show  
 334 the opposite behaviour. C-decreasing with P is due to the fact that both CO and  $CO_2$  have  
 335 solubility at C-saturation that decrease with increasing P (Stanley et al., 2014; Li et al., 2017;  
 336 Eguchi et al., 2018). For strongly hydrated samples, the C-solubility increases with P because  
 337 our modelling implies that  $CH_4$  is increasingly stabilized. This effect is data-driven since it  
 338 results from the fitted values as described in section 3, but it must also reflect the volume change  
 339 of the homogeneous reaction:



342 The volumes of the  $H_2O$  and  $CO_2$  components and their P-T dependences are well-known and  
 343 range, from 1 to 10 GPa, from 30 to 10 cc/mol and 34 to 22 cc/mol, respectively (ie. Gaillard  
 344 et al., 2019). The volume of  $CH_4$  and CO are, however, unknown. The solubility (ie. fluid-melt

345 equilibria) work of Ardia et al. (2014) and Armstrong et al. (2015) provides clues in the P range  
346 1-5 GPa, that allowed us to estimate  $V_{\text{CH}_4} \sim 27$  cc/mol and  $V_{\text{CO}} \sim 22$  cc/mol. The molar volume  
347 of  $\text{H}_2$  is given in Hirschmann et al. (2012),  $V_{\text{H}_2} = 11$ cc/mol. The volume changes of eq. (17) is  
348 ca. 2cc at ca. 1 GPa and may strongly evolve negative with increasing P, given the high  
349 compressibility of dissolved  $\text{H}_2\text{O}$ . We recall that the compressibility of  $\text{CH}_4$  is unknown. We  
350 expect similar P-evolution for eq. (18) given the poor compressibility of  $\text{CO}_2$  vs  $\text{H}_2\text{O}$ . We admit  
351 that independent and robust rationalization of the fact that  $\text{CH}_4$  must dominate H-bearing  
352 systems at HP is needed. At this stage, our model, that is data driven, cannot accurately account  
353 for volume changes with P. Our sensitivity analyses make this clear (supplementary section).  
354 The relatively simple formalism we adopted is justified by its capacity to capture the C-  
355 solubility in the experimentally calibrated P-T-f $\text{O}_2$ -f $\text{H}_2\text{O}$  parameter space.

356 A noteworthy feature is visible in figure 1b with the P extrapolation of our model: C-content in  
357 H-poor silicate melts at C-saturation must first decrease with increasing P in the range 1-20  
358 GPa (the domain where CO and  $\text{CO}_2$  dominate) and then increase at higher P because of  $\text{CH}_4$   
359 formation. Note that the inflexion P depends on the  $\text{H}_2\text{O}$  content (ie. 20 GPa for 50 ppm  $\text{H}_2\text{O}$ ,  
360 10 GPa for 200 ppm  $\text{H}_2\text{O}$  and 5 GPa for 500 ppm  $\text{H}_2\text{O}$ , the latter is not shown in fig. 1b). We  
361 predict that above 35 GPa (though we calculate large uncertainties at such high P), C-content  
362 should be in the range 100-60,000 ppm, depending on the  $\text{H}_2\text{O}$  content of the silicate melts. In  
363 spite of the large uncertainties, this extrapolation is consistent with the data of Fischer et al.  
364 (2020). Fischer et al (2020) data cannot be used in our calibration database because the H-  
365 content in their silicate melts is unknown but they nevertheless reported RAMAN spectra  
366 showing that  $\text{CH}_4$  is the only C-species detected in their sample. This give credence to our  
367 speciation model, but independent partial volume data and/or C-solubility experiments at high  
368 P are needed.

369

370 4.3.H-speciation and partitioning in P-T-fO<sub>2</sub> space

371 The H metal-silicate partition coefficient is also implicitly controlled by the C-O-H speciation  
372 and its P-T-fO<sub>2</sub> dependence. Figure 2 shows both experimental data and a range of calculation  
373 covering the relevant P-T-fO<sub>2</sub>-fH<sub>2</sub>O conditions. Figure 2a illustrates the fO<sub>2</sub> effect on H  
374 partitioning. This figure reveals two regimes:

- 375 - at oxidizing conditions,  $D_H^{\text{METAL/SILICATE}}$  increases as fO<sub>2</sub> decreases, which reflects the  
376 following reaction  $\text{H}_2\text{O}^{\text{SILICATE}} = 2 \text{H}^{\text{METAL}} + \frac{1}{2} \text{O}_2$   
377 - at reducing conditions,  $D_H^{\text{METAL/SILICATE}}$  increases as fO<sub>2</sub> decreases, which reflects the  
378 following reaction:  $\text{CH}_4^{\text{SILICATE}} + \text{O}_2 = 4 \text{H}^{\text{METAL}} + \text{CO}_2^{\text{SILICATE}}$

379 The reaction  $\text{H}_2^{\text{SILICATE}} = 2 \text{H}^{\text{METAL}}$  is necessarily operating but its effect (that should yield no  
380 fO<sub>2</sub> dependence) is weak in figure 2a.

381 The P effects are highlighted in figure 2b. Increasing P makes H more siderophile (as observed  
382 by Clesi et al, 2018 and Malavergne et al 2019), but this is strongly dependant on the fO<sub>2</sub>, T  
383 and the total H-content (see also Fig.2c). These effects are consistent with the recent HP-HT  
384 experimental study of Tagawa et al (2021) and the molecular dynamics studies of Li et al.  
385 (2020) and Yuan and Steinle-Neumann (2020) conducted on C-free systems that reported  
386 increasing P makes H sensibly more siderophile. At ca. 20 GPa, however, the calculated  $D_H$   
387 values reach a sort of plateau or an inflexion point, indicating the domain where CH<sub>4</sub> dominates  
388 in the silicate melt (see also fig. 1b for corresponding inflexion in the C-solubility vs P plot).  
389 Such an inflexion is obviously not described in the recent works cited above on C-free systems.

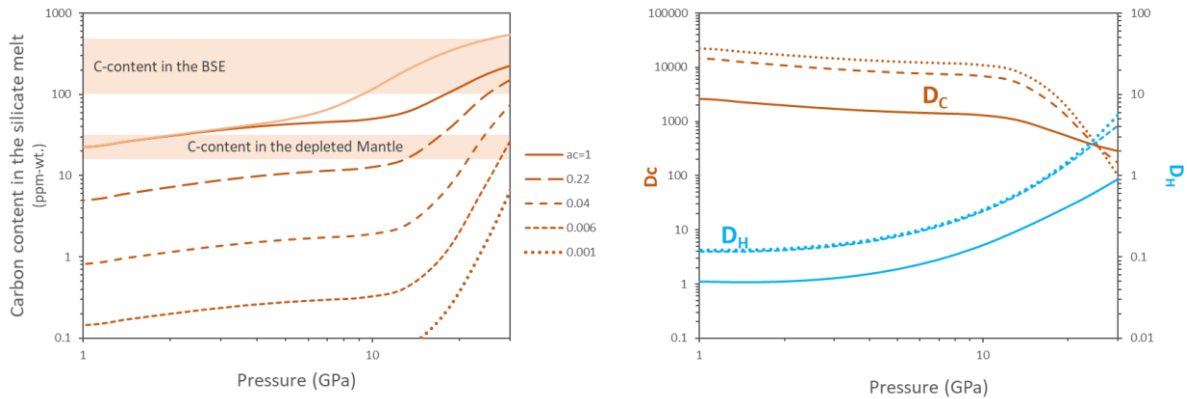
390 Figure 2c shows that lowering H-content in the silicate melt makes H more siderophile. This  
391 dependence of H-partitioning on H-content is also described in Li et al (2020) for a C-free  
392 system but not in other studies (Okuchi, 1998; Clesi et al., 2018; Malavergne et al., 2019). The  
393 effect of the H content is twofold: first, in reactions (13) and (15), ruling H-partitioning, 1 mole

394 of H-bearing species in the silicate melt reacts into 2 or 4 moles of H in the metal, a  
395 stoichiometry implying that the partitioning changes with H-content; second, the relationship  
396 between H<sub>2</sub>O mole fraction in the silicate and activity of H<sub>2</sub>O is a square function, which cancels  
397 the stoichiometric effect for reaction 15 at low P (ie. when all H is H<sub>2</sub>O). Figure 2c shows that  
398 the effect of H-content is critical at high P and low fO<sub>2</sub> conditions, where CH<sub>4</sub> dominates. At  
399 low P, where H<sub>2</sub>O dominates the H-speciation, the effect of H-content is insignificant. All this  
400 implies that the experiments must be collected in the expected range of H-content of the magma  
401 ocean in order to be directly applicable. The range of H<sub>2</sub>O content of the bulk silicate Earth  
402 given in Marty (2012) (1000-3000 ppm H<sub>2</sub>O, ca. 100-300 ppm H) and in Hirschmann (2018)  
403 (620-800 ppm H<sub>2</sub>O, ca. 60-80 ppm H) is the domain where small changes in the H-content of  
404 the silicate melt is predicted to have an important effect on H metal-silicate partitioning. Most  
405 current experimental data have been conducted above this range of H-content (Fig. 2c).

#### 406 4.4.C-undersaturation at variable pressures

407 Calculations in fig 1-3 are conducted for C activity of unity (i.e., graphite/diamond-bearing  
408 systems), however, in the absence of graphite/diamond, the activity of C is < 1 in metal, and  
409 hence activity-composition models are required to quantify C partitioning between metal and  
410 silicate. Such models must be confronted to experimental data at pressure. The experimental  
411 work of Kuwahara et al. (2019) provided C-partitioning data at C-undersaturation.  
412 Unfortunately, these experiments contain as much N as C, implying that the metal is a ternary  
413 Fe-C-N with complex activity-composition relationships. Furthermore, these experiments are  
414 massively contaminated with B (several wt % from the experimental assemblage). This makes  
415 it difficult to use the Kuwahara et al. (2019) data as absolute C-partitioning data. Nevertheless,  
416 this experimental work indicates that C tends to become less siderophile as the activity of C in  
417 the metal is reduced. Note that the existing low P activity-composition relationships for C in  
418 Fe-C (see supplementary section) implies that C should become more siderophile as C-activity

419 decreases (the activity coefficient of C in Fe-metal increases as C-activity increases). This effect  
 420 is actually visible in figure 4b, where  $D_C^{\text{metal-silicate}}$  is higher for C-undersaturated cases at  $P < 10$   
 421 GPa. At higher  $P$ , when  $\text{CH}_4$  dominates, we notice an inversion of the effect of C-activity on  
 422  $D_C^{\text{metal-silicate}}$ . Here (Fig. 4b), the calculation is done for a fixed  $H_{\text{tot}}$  content (80 ppm H that is the  
 423 Bulk Silicate Earth H-content after Hirschmann, 2018), and this H is essentially balanced  
 424 between  $\text{H}_2\text{O}$  and  $\text{CH}_4$ . When  $\text{CH}_4$  is involved, the total C-content does not only depend on  $a_C$   
 425 and  $f\text{O}_2$ , but it also depends on the fraction of  $\text{H}_2\text{O}$  (eq. 7). For a system containing more  $H_{\text{tot}}$ ,  
 426 the crossover, described in fig. 4b at 10 GPa, must occur at lower  $P$ . This simple analysis reveals  
 427 that the effect of C-undersaturation on  $D_C^{\text{metal-silicate}}$  is complex since it depends on  $P$  and H-  
 428 contents in the silicate melt.



429  
 430 *Figure 4: The effect of  $P$  and C-activity on the C-solubility in silicate melt and on the metal-*  
 431 *silicate partitioning for C and H. As  $P$  increases from 1 to 30 GPa,  $T$  increases from 1600 to*  
 432 *2800°C. The H content is fixed to 80 ppm H (H-mantle after Hirschmann, 2018) in all curves*  
 433 *but the pink one on the top of the left panel, which shows C-solubility for a silicate melt*  
 434 *containing 160 ppm H.*

435 The effect of C-activity on  $D_H^{\text{metal-silicate}}$  is also addressed in Figure 4b, showing that H becomes  
 436 increasingly siderophile as the metal C-activity is reduced. This is consistent with the results  
 437 from the four available experimental studies (Okuchi, 1998; Clesi et al., 2018; Malavergne et  
 438 al., 2019; Tagawa et al, 2021), indicating that H is more siderophile in C-free ( $D_H > 1$ ) than in

439 C-saturated systems ( $D_H < 1$ ). This is also consistent with the molecular dynamics data of Li et  
440 al. (2020) which demonstrate that partitioning of H between molten metal and silicate melt  
441 exceeds 10 at extreme P-T conditions (up to  $> 100$  GPa and  $> 3000^\circ\text{C}$ ) in C-free systems. The  
442 driving force that makes H increasingly siderophile with C-undersaturation is captured by the  
443 following equilibrium, which dominates the metal-silicate partitioning of H at high P:



445 As the activity of C in metal is reduced, the above equilibrium is shifted to the right-hand side,  
446 making H more siderophile.

447 The behaviour of C-O-H species during metal – silicate equilibria under C-undersaturated  
448 conditions is currently under-constrained by experimental surveys. Whereas we are confident  
449 of the effect of C-undersaturation on  $D_H$  described here, its effect on  $D_C$  appears to be multiple  
450 and more difficult to capture. Experiments with C under-saturation conditions are essential to  
451 test the validity of the important conclusions reached at this stage.

452

## 453 **5. Geochemical Implications for mantle - core differentiation on Earth**

454 A series of calculations investigate the fate of H and C in the P-T-X parameter space permitted  
455 by our model. We limit our calculations to 30 GPa. Outside of this P-range, excessively large  
456 uncertainties prevent any sound discussion. These calculations nevertheless allow us to discuss  
457 the effect of variable values of C-activities and the effect of P. We consider two endmember  
458 cases:

459 (i) metal efficiently sinks and ponds at the base of the magma ocean (fig. 5, top-left side).

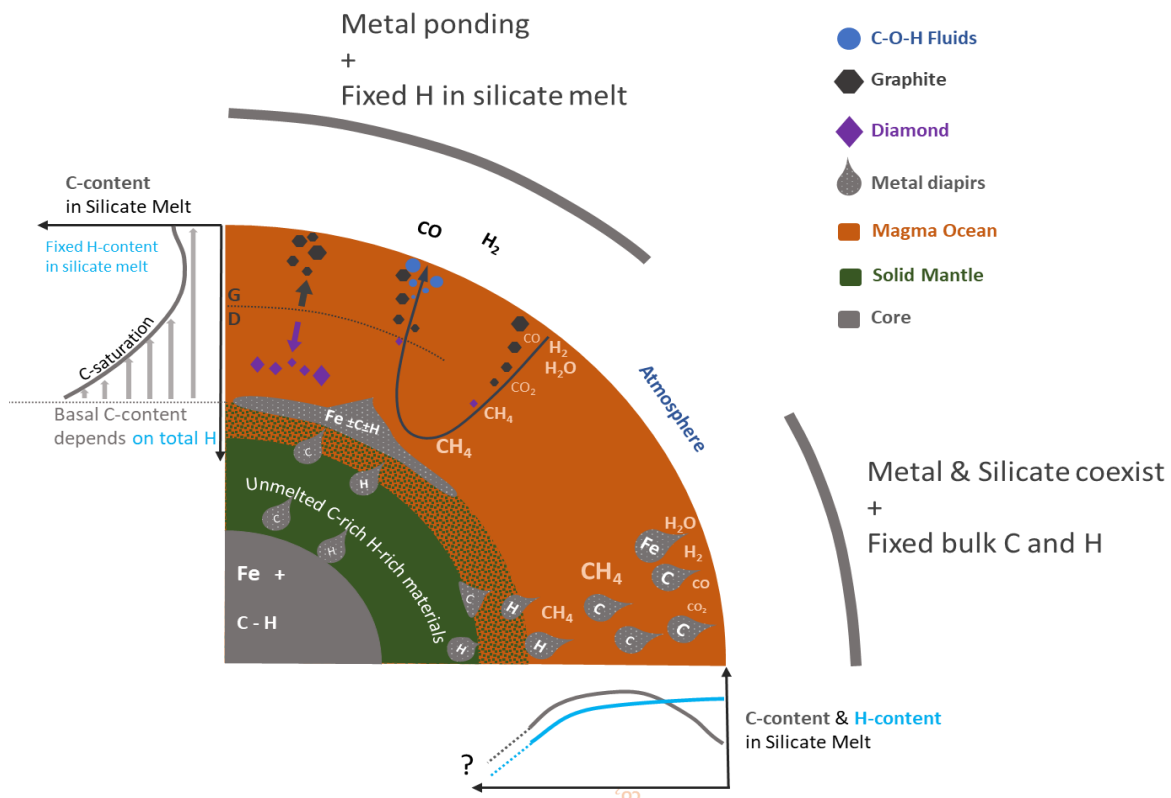
460 The C and H partitioning at high-P high-T will control the activity of C and H in the entire  
461 magma ocean.

462 (ii) metal and silicate coexist all along the magma ocean vertical section (fig. 5, bottom-  
463 right side); in that case, C and H partition between metal and silicate at all depths.

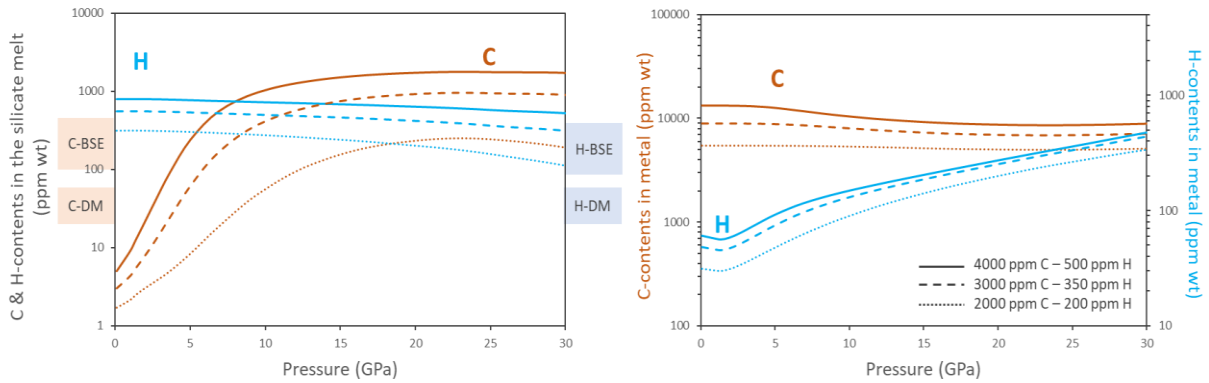
464 Figure 4a shows the C-solubility in silicate melt vs. P (or depth) in a magma ocean. Variable  
465 values of C-activity are computed, whereas the H-content in the magma is fixed to 80 ppm H  
466 (Bulk Silicate Earth after Hirschmann, 2018; in addition, a sensitivity test shows the effect of  
467 doubling this amount of H). This means that we neglect H degassing as suggested by previous  
468 studies (Sossi et al., 2020; Gaillard et al., 2021). The C solubility increases with increasing P  
469 from ca.  $20 \pm 5$  ppm at 1 GPa to a maximum value of ca.  $293 \pm 95$  ppm at 30 GPa-2800°C. In the  
470 latter case, C is mostly as CH<sub>4</sub>. Accordingly, most H (ie. 70 ppm H) is in the CH<sub>4</sub> form. The C  
471 content in the basal magma ocean is therefore controlled by the H availability. At low P, in  
472 contrast, most H occurs as H<sub>2</sub>O (75 ppm H), most C occurs as dissolved CO (max. 13 ppm) and  
473 the remaining C occurs as CO<sub>2</sub> (4 ppm). A first conclusion must be highlighted here, the depth  
474 of the magma ocean controls its C content, implying that shallow magma oceans must have low  
475 C-contents (~ca. tens of ppm), whereas deep magma oceans enable high C-content (ca. >100  
476 ppm C). At such high-P, the affinity of C for the metal is not as strong as at low P (Fig. 4b)  
477 implying that C assimilation by the core in large planet must weaken, whereas the core of small  
478 planets must massively take C. This point is consistent with the experimental model of Fischer  
479 et al (2020). The second conclusion is that convection-driven upward transfer of such C-rich  
480 basal magma ocean regions implies decompression-induced speciation changes, with C & H,  
481 shifting from CH<sub>4</sub>-dominant to CO-H<sub>2</sub>O dominant during ascent. Such a speciation change is  
482 not redox neutral and must consume oxygen (lowering the  $fO_2$ ). In addition, as indicated in  
483 figure 4a, the solubility of C must decrease, implying that C saturation may be reached as the  
484 melt moves toward the surface of the magma ocean. This scenario is illustrated on the left part  
485 of figure 5, where a vertical gradient in C-solubility causes C-saturation in upwelling regions  
486 of the magma ocean, while downwelling regions must dissolve graphite or diamond. The C-



487 content in the basal silicate melt, where deep metal-silicate equilibration takes place, is  
 488 controlled by the availability of H to form CH<sub>4</sub>. In the case of figure 4, we recall that the H  
 489 content in the silicate melt is constant (80 ppm), and it corresponds to the H-content in the bulk  
 490 silicate Earth. If this H content is doubled, it greatly impacts the C-solubility in the P domain  
 491 where CH<sub>4</sub> dominates (fig. 4a). Marty (2012) reported much greater values (up to 290 ppm)  
 492 than Hirschmann (2018) for the H-contents in the BSE. We therefore conclude that a large range  
 493 of C-solubility in the basal magma ocean is possible (from ca. 200 to 1000 ppm) reflecting the  
 494 uncertainties in H-content in the BSE (fig. 4a). In any case, we see that the calculated range of  
 495 C-contents is comparable to the C-content of the depleted mantle in the P-range < 10 GPa and  
 496 with C-content of the BSE (ie. Hirschmann, 2018; Marty, 2012) at P > 10 GPa.



497  
 498 *Figure 5: Diagram illustrating the two simulated magma ocean configurations, involving a*  
 499 *basal layer of metal (top-left) and metal droplets being spread in the magma ocean (bottom-*  
 500 *right). The top-left case is simulated in fig. 4, whereas the bottom-right one is shown in fig.6.*



501

502 *Figure 6: The fate of C & H in a magma ocean that contains Fe-metal at all depth. Here, we*  
 503 *fixed the bulk C and H contents (in metal + silicate) as indicated in the legend. C solubility in*  
 504 *the magma ocean increases with increasing P until a critical depth, where H becomes*  
 505 *siderophile. Beyond this threshold P, we propose that the magma may get increasingly*  
 506 *desiccated. P-T evolution similar to figure 4.*

507 As illustrated in the right side of figure 5, if one considers that metal and silicate coexist all  
 508 along the magma ocean vertical section, C-saturation is, in contrast, unlikely since the metal  
 509 takes most C. We simulated in figure 6 such a case with fixed bulk C and H contents along the  
 510 magma ocean profile (several runs were done with 4000-3000-2000 ppm C and 500-350-200  
 511 ppm H). Here, we focus on a somewhat simple, but increasingly popular model of accretion for  
 512 planet Earth made up mainly of enstatite chondrites (eg. Javoy et al., 2010; Piani et al., 2020).  
 513 Enstatite chondrites contain 4000 ppm C and 490 ppm H (Piani et al., 2020). We conducted  
 514 calculations at a fixed  $fO_2$  of IW-2 (no significant difference with simulations done at IW-4)  
 515 for a set of P-T conditions similar to figure 4. At low pressure (ie. less than 5GPa), one sees  
 516 that most C is sequestered in the molten metal phase, leaving only a few tens of ppm C in the  
 517 silicate melt. In contrast, H is mainly partitioned in the silicate melt. As P increases, C becomes  
 518 less siderophile, reaching contents of ca. 200-1000 ppm-wt. in the silicate magma ocean,  
 519 depending on the H content, at 20 GPa. This is because  $CH_4$  becomes increasingly stable. In  
 520 the meantime, H becomes increasingly siderophile. As P increases further, this can lead to the

521 dehydrogenation of the silicate melt, which may evolve dry at  $P > 30$  GPa, but our model does  
522 not allow calculations to be conducted at such pressure due to too large uncertainties. Whereas  
523 we are confident in the enhanced stability of  $\text{CH}_4$  at high  $P$ , and the geochemical consequences  
524 we briefly expose here, reducing the uncertainties of predicted values is a necessity in order to  
525 quantitatively link chondritic C-H abundances and the distribution of these elements during  
526 the magma ocean stages. In order to do so, we need independent constraints on C-O-H species  
527 compressibility and  $a\text{-X}$  relationships in a metal that become multicomponent and increasingly  
528 O-rich as pressure increase (eg. Tagawa et al., 2021)

529

## 530 **6. Conclusions and perspectives**

531 A growing body of experimental and molecular dynamics data have recently been produced in  
532 the literature on the partitioning of C and H during metal – silicate equilibria. Whereas these  
533 data originated from a number of laboratories, used different methods and produced different  
534 results, the modelling carried out here shows that all the data can be reconciled within the  
535 framework of a melt speciation model, involving the C-H-species  $\text{H}_2\text{O}$ ,  $\text{H}_2$ ,  $\text{CO}_2$ ,  $\text{CO}$ , and  $\text{CH}_4$   
536 dissolved in a silicate melt. The dependence of the stability of these species on  $P$ ,  $T$  and  $f\text{O}_2$  can  
537 be related to previously determined values of H and C metal – silicate partition coefficients.

538 The use of this model allows us to distinguish two types of magma ocean: shallow and deep  
539 ones. In shallow magma oceans, C is strongly siderophile, while H is not siderophile. In deep  
540 magma oceans, C evolves to become less siderophile, while H becomes increasingly  
541 siderophile. The partitioning of H into metal depends on both  $P$  and C activity. In a C-poor,  
542 deep magma ocean, H incorporation into the core could lead to desiccation of the magma ocean.

543 Experimental and MD tests of this model are, however, needed since there are not enough  
544 constraints at this stage in certain regions of the parameter space (eg. low C-activity, high  $P$ )

545 /low H content). Investigation of both C and H during partitioning are required since these are  
546 coupled through speciation relationships. This model is ultimately expected to evolve towards  
547 a multicomponent mixture taking into account all possible stoichiometric interactions between  
548 species in the C-H-O-N-S system (eg. Tsuno et al., 2018).

549

## 550 **7. References**

551 Ardia P., Hirschmann MM, Withers AC, Stanley BD, 2014. Solubility of CH<sub>4</sub> in a synthetic  
552 basaltic melt, with applications to atmosphere–magma ocean–core partitioning of volatiles  
553 and to the evolution of the Martian atmosphere. *Geochimica et Cosmochimica Acta* 114, 52-  
554 71.

555 Armstrong, L.S., et al., 2015. The speciation of carbon, nitrogen, and water in magma oceans  
556 and its effect on volatile partitioning between major reservoirs of the Solar System rocky  
557 bodies. *Geochim. Cosmochim. Acta* 171, 283-302.

558 Badro, J., Brodholt, J.P., Piet, H., Siebert, J., Ryerson, F.J., 2015. Core formation and core  
559 composition from coupled geochemical and geophysical constraints. *Proc. Natl Acad. Sci. USA*  
560 112, 12310–12314.

561 Chi, H., Dasgupta, R., Duncan, M.S., Shimizu, N., 2014. Partitioning of carbon between Fe-  
562 rich alloy melt and silicate melt in a magma ocean – implications for the abundances and origins  
563 of volatiles in Earth, Mars and Moon. *Geochim. Cosmochim. Acta* 139, 447–471.

564 Clesi, V., Bouhifd, M.A., Bolfan-Casanova, N., Manthilake, G., Schiavi, F., Raepsaet, C.,  
565 Bureau, H., Khodja, H., Andrault, D., 2018. Low hydrogen contents in the cores of terrestrial  
566 planets. *Sci. Adv.* 4, e1701876.

567 Dalou C., Hirschmann M. M., Jacobsen S. D., Le Losq, C., 2019. Raman spectroscopy study  
568 of C-O-H-N speciation in reduced basaltic glasses: implications for reduced planetary mantles.  
569 *Geochim. Cosmochim. Acta* 265, 32–47.

570 Dasgupta, R., Chi, H., Nobumichi, S., Buono, A.S., Walker, D., 2013. Carbon solution and  
571 partitioning between metallic and silicate melts in a shallow magma ocean: implications for the  
572 origin and distribution of terrestrial carbon. *Geochim. Cosmochim. Acta* 102, 191–212.

573 Duncan, M. S., Dasgupta, R., Tsuno, K. (2017). Experimental determination of CO<sub>2</sub> content at  
574 graphite saturation along a natural basalt-peridotite melt join: Implications for the fate of carbon  
575 in terrestrial magma oceans. *Earth Planet. Sci. Lett.* 466, 115-128.

576 Eguchi, J., Dasgupta, R., 2017. CO<sub>2</sub> content of andesitic melts at graphite saturated upper  
577 mantle conditions with implications for redox state of oceanic basalt source regions and  
578 remobilization of reduced carbon from subducted eclogite. *Contributions to Mineralogy and*  
579 *Petrology* 172, 12.

580 Eguchi, J., Dasgupta, R., 2018. A CO<sub>2</sub> solubility model for silicate melts from fluid saturation  
581 to graphite or diamond saturation, *Chem. Geol.*, 487, 23–38.

582 Fischer, R., et al., 2020. The carbon content of Earth and its core *PNAS* 117 (16) 8743-8749.

583 Fichtner C.E., et al., 2021. Carbon partitioning between metal and silicate melts during Earth  
584 accretion. *Earth and Planetary Science Letters*, 554, 116659,  
585 <https://doi.org/10.1016/j.epsl.2020.116659>

586 Gaillard, F., et al. (2019). The Link between the Physical and Chemical Properties of Carbon-  
587 Bearing Melts and Their Application for Geophysical Imaging of Earth's Mantle. In B.  
588 Orcutt, I. Daniel, & R. Dasgupta (Eds.), *Deep Carbon: Past to Present* (pp. 163-187).  
589 *Cambridge: Cambridge University Press.*

590 Gaillard, F. et al. The Diverse Planetary Ingassing/Outgassing Paths Produced over Billions  
591 of Years of Magmatic Activity. *Space Sci. Rev.* 217, 1-54 (2021)

592 Greenwood, R.C., Barrat J-A, Miller M.F., et al., 2018. Oxygen isotopic evidence for accretion  
593 of Earth's water before a high-energy Moon-forming giant impact. *Science Advances* 4 (3):  
594 eaao5928.

595 Grewal, D.S., Dasgupta, R., Sun, C., Tsuno, K., Costin, G., 2019. Delivery of carbon, nitrogen,  
596 and sulfur to the silicate Earth by a giant impact. *Sci. Adv.* 5, eaau3669.

597 Hirschmann, M.M., 2012a. Magma ocean influence on early atmosphere mass and composition.  
598 *Earth Planet. Sci. Lett.* 341-344, 48–57.

599 Hirschmann, M.M., et al., 2012b. Solubility of molecular hydrogen in silicate melts and  
600 consequences for volatile evolution of terrestrial planets. *Earth and Planetary Science Letters*  
601 345-348 38–48.

602 Hirschmann, M.M., Comparative deep Earth volatile cycles: The case for C recycling from  
603 exosphere/mantle fractionation of major (H<sub>2</sub>O, C, N) volatiles and from H<sub>2</sub>O/Ce, CO<sub>2</sub>/Ba,  
604 and CO<sub>2</sub>/Nb exosphere ratios. *Earth Planet. Sci. Lett.* 502, 262–273 (2018)

605 Iacono-Marziano, G., Morizet, Y., Le-Trong, E., Gaillard, F., 2012. New experimental data and  
606 semi-empirical parameterization of H<sub>2</sub>O-CO<sub>2</sub> solubility in mafic melts. *Geochim. Cosmochim.*  
607 *Acta* 97, 1-23.

608 Javoy, M., Kaminski, E., Guyot, F., Andrault, D., Sanloup, C., Moreira, M., Labrosse, S.,  
609 Jambon, A., Agrinier, P., Davaille, A., Jaupart, C., 2010. The chemical composition of the  
610 Earth: enstatite chondrite models. *Earth Planet. Sci. Lett.* 293, 259–268.

611 Kadik, A.A., Koltashev, V.V., Kryukova, E.B., Plotnichenko, V.G., Tsekhonya, T.I.,  
612 Kononkova, N.N., 2014. Solution behavior of C-O-H volatiles in FeO-Na<sub>2</sub>O-Al<sub>2</sub>O<sub>3</sub>-SiO<sub>2</sub> melts  
613 in equilibrium with liquid iron and graphite at 4 GPa and 1550 °C. *Geochem. Int.* 52, 707–725.

614 Kuwahara, H., Itoh, S., Nakada, R., Irifune, T., 2019. The effects of carbon concentration and  
615 silicate composition on the metal–silicate partitioning of carbon in a shallow magma ocean.  
616 *Geophysical research letters*. doi: 10.1029/2019GL084254.

617 Li, Y., Dasgupta, R., Tsuno, K., 2015. The effects of sulfur, silicon, water, and oxygen fugacity  
618 on carbon solubility and partitioning in Fe-rich alloy melt-silicate melt systems at 3 GPa and  
619 1600 °C – Implications for core-mantle differentiation and degassing of magma oceans and  
620 reduced planetary mantles. *Earth Planet. Sci. Lett.* 415, 54-66.

621 Li, Y., Dasgupta, R., Tsuno, K., Monteleone, B., Shimizu, N., 2016. Carbon and sulfur budget  
622 of the silicate Earth explained by accretion of differentiated planetary embryos. *Nat. Geosci.* 9,  
623 781–785.

624 Li, Y., Dasgupta, R., Tsuno, K., 2017. Carbon contents in reduced basalts at graphite saturation:  
625 Implications for the degassing of Mars, Mercury, and the Moon. *Journal of Geophysical*  
626 *Research - Planets* 122, doi:10.1002/2017JE005289.

627 Li, Y., Vočadlo, L., Sun, T., Brodholt, J.P., 2020. The Earth’s core as a reservoir of water. *Nat.*  
628 *Geosci.* 13, 453–458.

629 Malavergne, V. et al., 2019. Experimental constraints on the fate of H and C during planetary  
630 core–mantle differentiation. Implications for the Earth. *Icarus* 321, 473–485.

631 Marty, B., 2012. The origins and concentrations of water, carbon, nitrogen and noble gases on  
632 Earth. *Earth Planet. Sci. Lett.* 313-314, 56-66.

633 Newcombe, M.E., Brett, A., Beckett, J.R., Baker, M.B., Newman, S., Guan, Y., Eiler, J.M. and  
634 Stolper, E.M., 2017. Solubility of water in lunar basalt at low pH<sub>2</sub>O. *Geochim. Cosmochim.*  
635 *Acta* 200, 330–352.

636 Okuchi, T., 1996. Hydrogen Partitioning into Molten Iron at High Pressure: Implications for  
637 Earth's Core. *Science* 278, 1781-1784.

638 Ohtani, E., Hirao, N., Kondo, T., Ito, M., Kikegawa, T., 2005. Iron–water reaction at high  
639 pressure and temperature, and hydrogen transport into the core. *Phys. Chem. Miner.* 32, 77–82.

640 Piani, L., et al., 2020. Earth's water may have been inherited from material similar to enstatite  
641 chondrite meteorites. *Science* 369, 1110-1113.

642 Rubie, D.C., et al., 2015. Accretion and differentiation of the terrestrial planets with  
643 implications for the compositions of early-formed Solar System bodies and accretion of water.  
644 *Icarus* 248, 89–108.

645 Sarafian, A.R., Nielsen, S.G., Marschall, H.R., et al., 2014. Early accretion of water in the inner  
646 solar system from a carbonaceous chondrite–like source. *Science* 346, 623–626.

647 Siebert, J., Badro, J., Antonangeli, D., Ryerson, F.J., 2012. Metal-silicate partitioning of Ni and  
648 Co in a deep magma ocean, *Earth Planet. Sci. Lett.* 321, 189-197.

649 Solomatova, N. V., Caracas, R., Manning, C.E., 2019. Carbon sequestration during core  
650 formation implied by complex carbon polymerization, *Nature Communications*, 10(1), 789,  
651 doi:10.1038/s41467-019-08742-9.

652 Stanley, B.D., Hirschmann, M.M., Withers, A.C., 2014. Solubility of C-O-H volatiles in  
653 graphite-saturated martian basalts. *Geochim. Cosmochim. Acta* 129, 54–76.

654 Tagawa, S., Sakamoto, N., Hirose, K. *et al.* Experimental evidence for hydrogen incorporation  
655 into Earth's core. *Nat Commun* **12**, 2588 (2021). <https://doi.org/10.1038/s41467-021-22035-0>



656 Tsuno, K., Grewal, D.S., R. Dasgupta, R., 2018. Core-mantle fractionation of carbon in Earth  
657 and Mars: The effects of sulfur. *Geochim. Cosmochim. Acta* 238, 477–495.

658 Wade, J, Wood, B.J., 2005. Core formation and the oxidation state of the Earth. *Earth Planet.*  
659 *Sci. Lett.* 236 78-95.

660 Wetzel, D.T., Rutherford, M.J., Jacobsen, S.D., Hauri, E.H., Saal, A.E., 2013. Degassing  
661 of reduced carbon from planetary basalts. *Proc. Natl. Acad. Sci. USA* 110,  
662 8010–8013.

663 Wood, B.J., Li, J., Shahar, A., 2013. Carbon in the core: Its influence on the properties of core  
664 and mantle. *Reviews in Mineralogy & Geochemistry*, 75, 231-250.

665 Yuan, L., Steinle-Neumann, G., 2020. Strong sequestration of hydrogen into the Earth's core  
666 during planetary differentiation. *Geophysical Research Letters*, 47, e2020GL088303.

667 Zhang, Y., Yin, Q. Z., 2012. Carbon and other light element contents in the Earth's core based  
668 on first-principles molecular dynamics. *PNAS* 109, 16579-16583.

669

## 670 **8. Acknowledgment**

671 This research is supported by the GASTON project (ANR-18-CE31-0021). G.R. is supported  
672 by the VOLTAIRE project (ANR-10-LABX-100-01). We acknowledge the careful reviews  
673 by M Hirschmann and Paolo Sossi.

674

675 **9. Supplementary information**

676

677 **H & C activity coefficient in metal**

678 The behaviour of H in metals is not thought to be ideal but its activity coefficient follows the  
679 empirical relationships given in Lob et al (2011):

680 
$$\log \gamma_H = 0.169 \times C^{METAL} - 0.2516 \quad (17)$$

681 Where  $C^{metal}$  stands for the mass fraction of C in metal. Activity-composition relationships for  
682 C in metals have been defined in the metallurgy literature (eg. Wang et al. 1991). These are  
683 used with the calculations for C-undersaturated systems below (see section 4.4). The presence  
684 of <20% Ni is not considered to affect the activity of H as shown by previous thermodynamic  
685 analyses of the 1-atm database (Jiang et al., 2011). We must specify at this stage that the non-  
686 ideality laws for H and C in the metal as suggested from 1-atm studies have not yet been verified  
687 by HP data. We suggest that specific HP experimental studies be devoted to this purpose (eg.  
688 Li et al., 2016 for C-S interactions in metals).

689

690 **Regressed parameters**

691 Regressed parameters and their uncertainties are shown in table S1. These constants can be used  
692 to compute the log K of each reactions as follows:

693 
$$\log K = -\frac{\Delta G_r}{RT} = \frac{A}{T} + B + C \times \frac{P}{T} + D \times NBO$$

694 In table S1, the A terms must be multiplied by 1000. Note that the C terms is in some cases  
695 modified as  $C^{mod} = C + C' \times P/T$  in order to allow the volume change of the reaction to change

696 with P and T. In most of these cases, the uncertainties are very large underlining the need of  
 697 getting robust compressibility data for C-O-H species in silicate melts.

698 Our procedure for getting uncertainties imply that these are not symmetrical so we give in table  
 699 S1 the lower and upper bound values for each fitted value.

700

701

702 Table S1: Regressed parameters and their upper and lower bounds. Units allow the log K of  
 703 each reaction to be calculated in molar ratios.

Reaction	Constant	Best fit	Bounds
<b>C metal</b>	<b>A2</b>	-0.487	-0.52 / -0.41
	<b>B2</b>	1.022	1.11 / 0.85
	<b>C2</b>	-0.006	-0.007 / -0.005
<b>CO2</b>	<b>A5</b>	-8.794	-9.3 / -8.5
	<b>B5</b>	-0.054	-0.35 / 0.1
	<b>C5</b>	-0.201	-0.6 / 0.05
	<b>C5'</b>	9.512	2 / 21
<b>CO</b>	<b>D5</b>	0.784	0.57 / 0.9
	<b>A6</b>	-1.658	-1.83 / -1.53
	<b>B6</b>	-2.220	-2.31 / -2.15
<b>CH4</b>	<b>C6</b>	-0.287	-0.38 / -0.2
	<b>A7</b>	-9.760	-9.96 / -9.62
	<b>B7</b>	0.019	-0.07 / 0.081
	<b>C7</b>	0.441	0.406 / 0.465
	<b>C7'</b>	-6.382	-16.8 / 0.9

<b>H2</b>	<b>A11</b>	-6.867	-20 / -6
	<b>B11</b>	-0.165	-4 / 0.25
	<b>C11</b>	-0.638	-4 / -0.3
	<b>A13</b>	15.470	12.8 / 16.6
	<b>B13</b>	0.612	-0.7 / 1.2
	<b>C13</b>	0.012	-0.35 / 0.15
<b>H metal</b>	<b>C13'</b>	7.085	-2 / 15

704

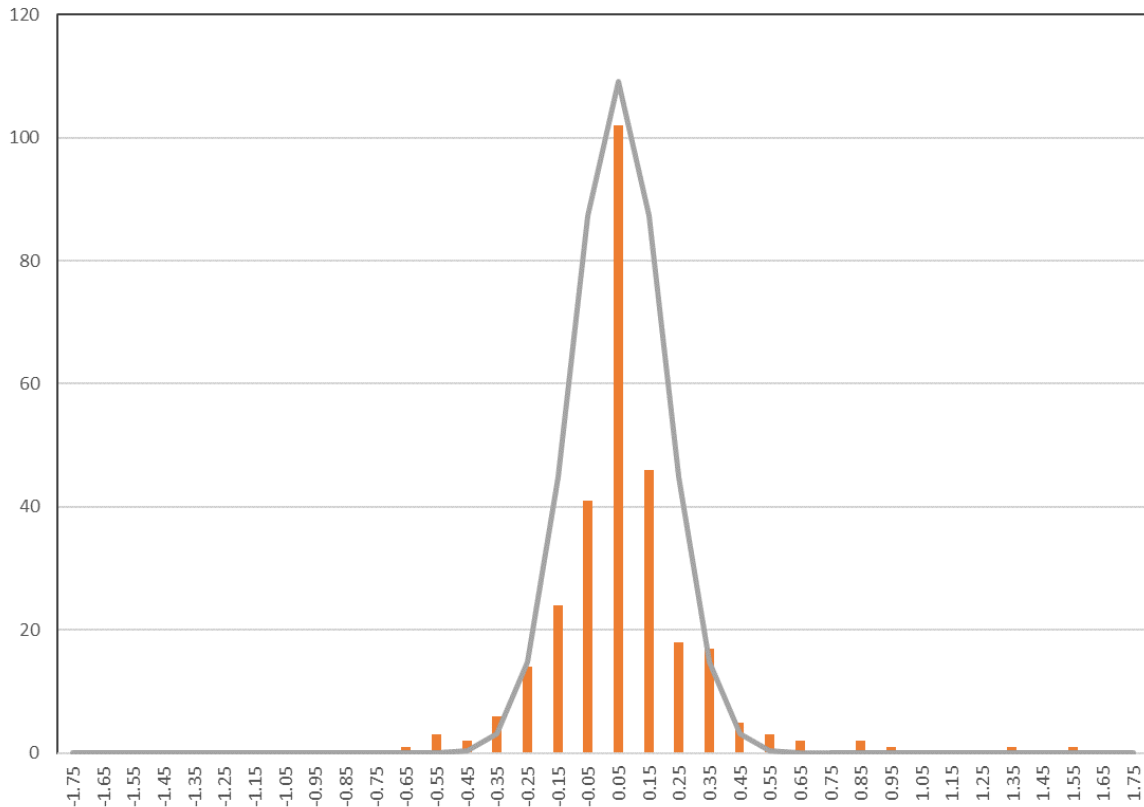
705 The online calculation tools use the numbers provided in table S1 to calculate the various  
706 equilibria. The uncertainty propagations use an average error (lower bound – upper bound  
707 divided by 2).

708 The ability of our model to reproduce the experimental observations has been quantified in  
709 figure S1, which shown the distribution of residues expressed as deviation per data, in fraction,  
710 expressed as follows:

$$711 \text{ Deviation} = (\text{observation} - \text{computed}) / \text{observation}$$

712 A value of 1 means that the misfit is 100 %. The distribution of residues (fig. S1) indicates a  
713 one sigma value of 0.15 (15 %), which explains the 30 % uncertainties (2 sigma) announced in  
714 section 4.1.

715

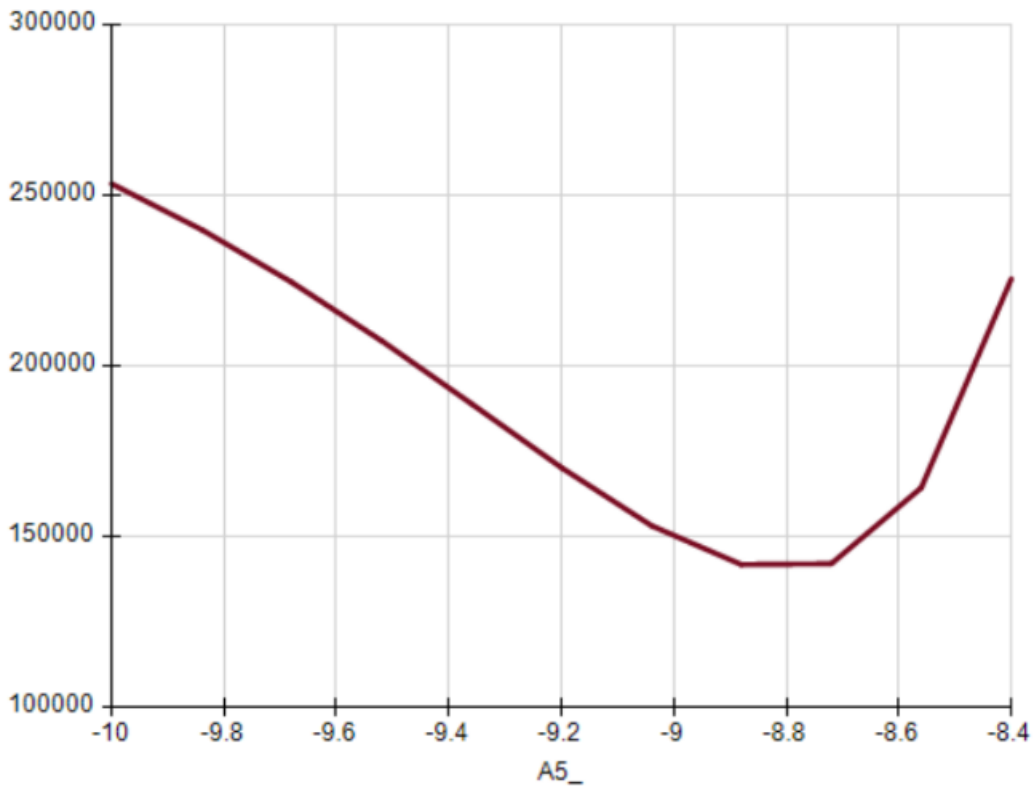


716

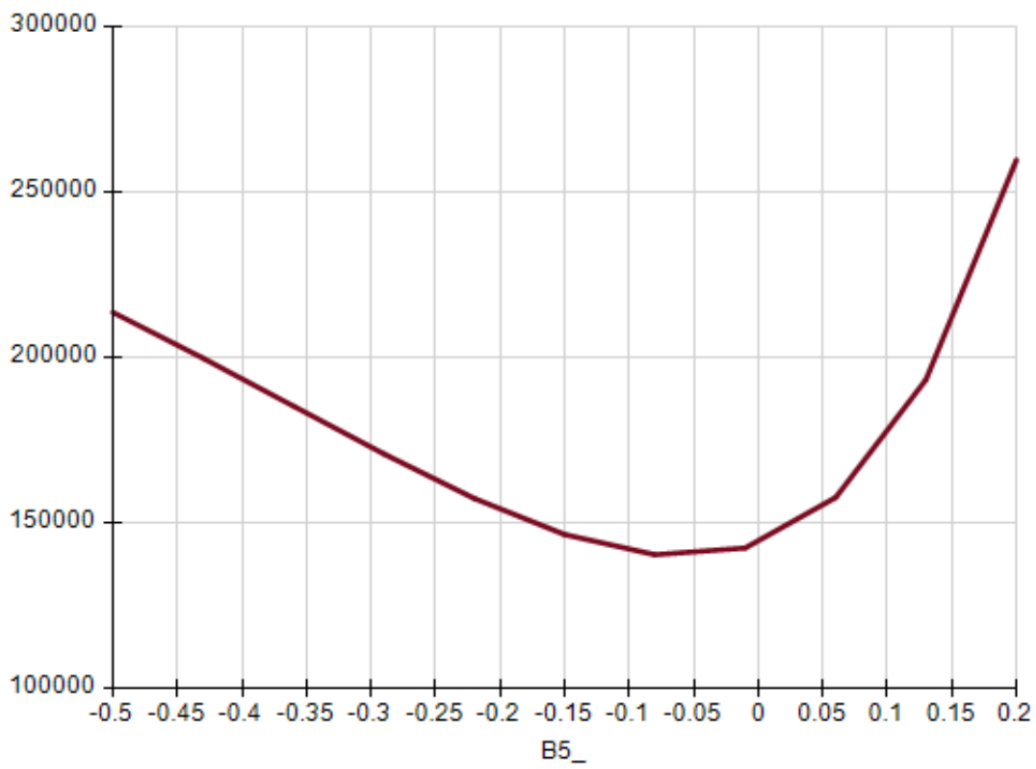
717 *Figure S1: Frequency diagram showing the distribution of misfit per data. The horizontal scale*  
 718 *is expressed as fraction of the value to fit. In practice, this must be read as more than 100*  
 719 *experimental observations are reproduced to within 5%. In grey is shown a log-normal curve*  
 720 *calculated for a 1-sigma of 0.15.*

721 Figure S2 illustrates the sensitivity tests for some of the regressed parameters. The values of  
 722 the Soptim function (residues normalized to experimental uncertainties) vary as the regressed  
 723 parameters are changed, with a minimum centred on the regressed values. In most cases, the  
 724 error a non-symmetrical. We considered that values of the Soptim function below 180,000 (30%  
 725 variation relative to the minimum) correspond to the acceptable range for the regressed  
 726 parameters.

727



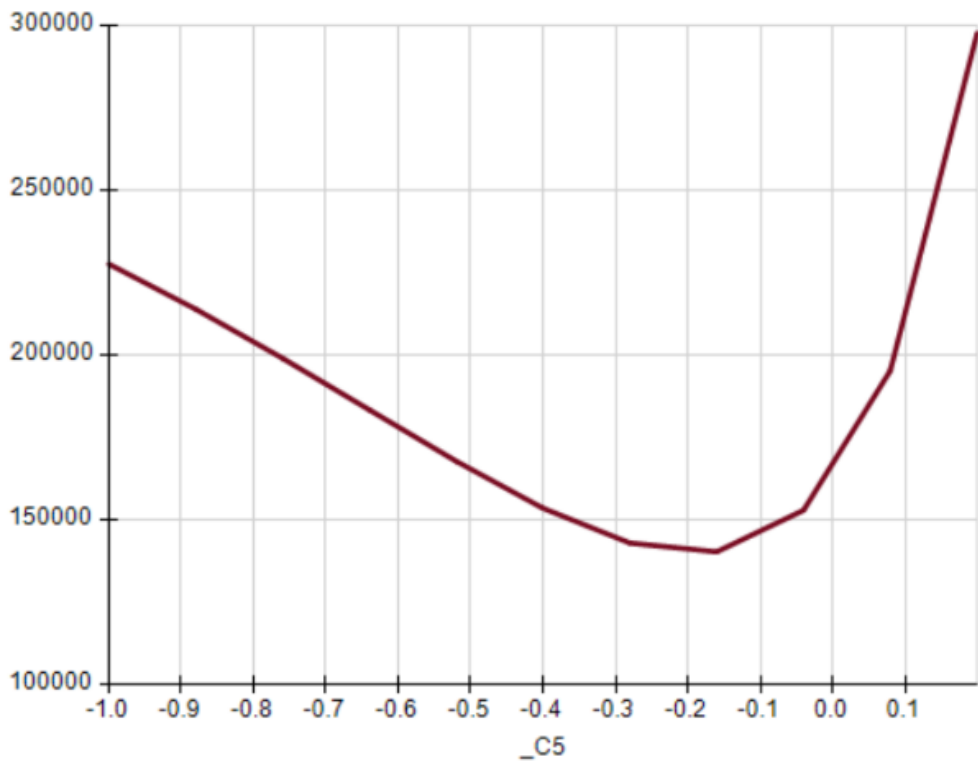
728



729

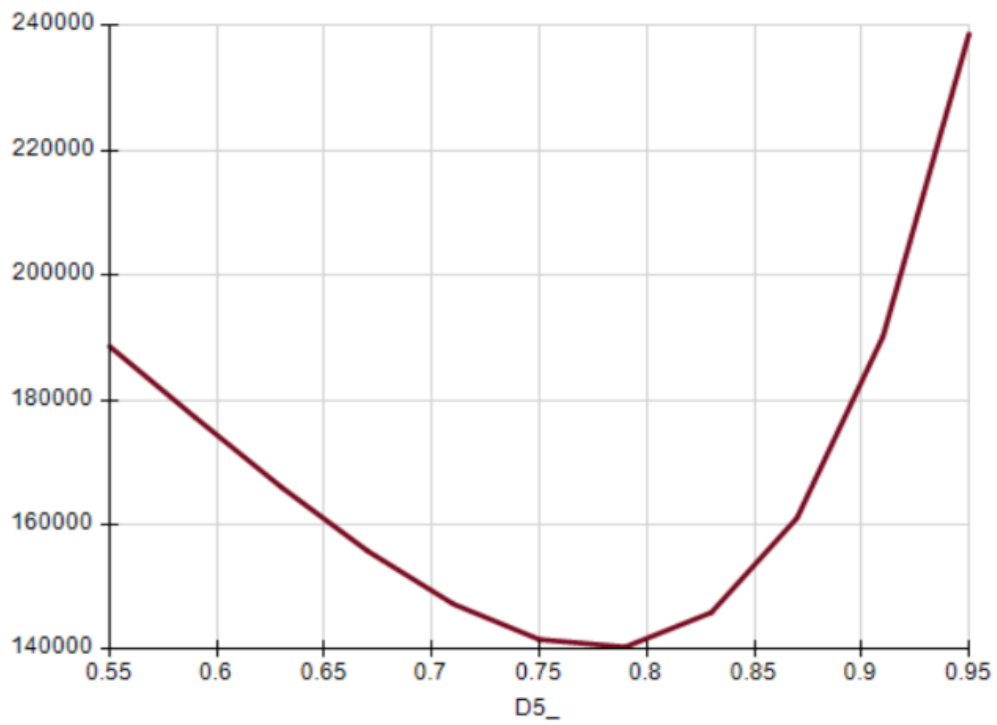
730

731



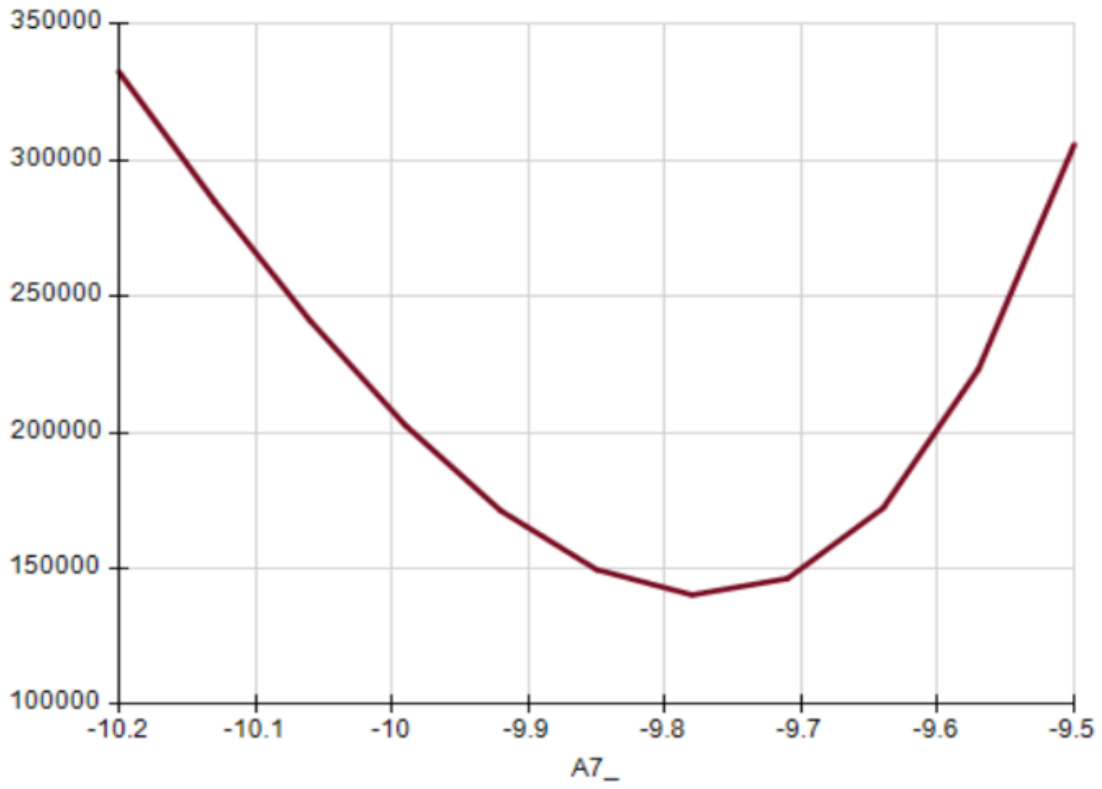
732

733



734

735

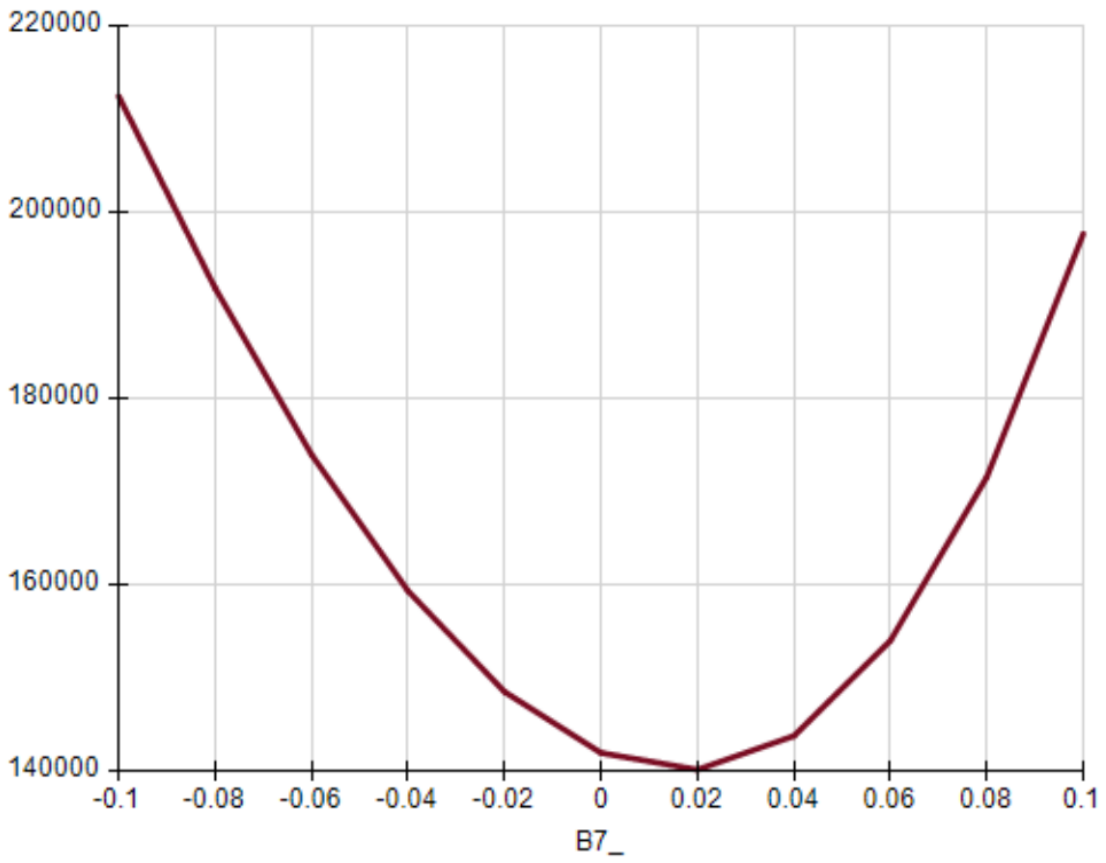


745

746

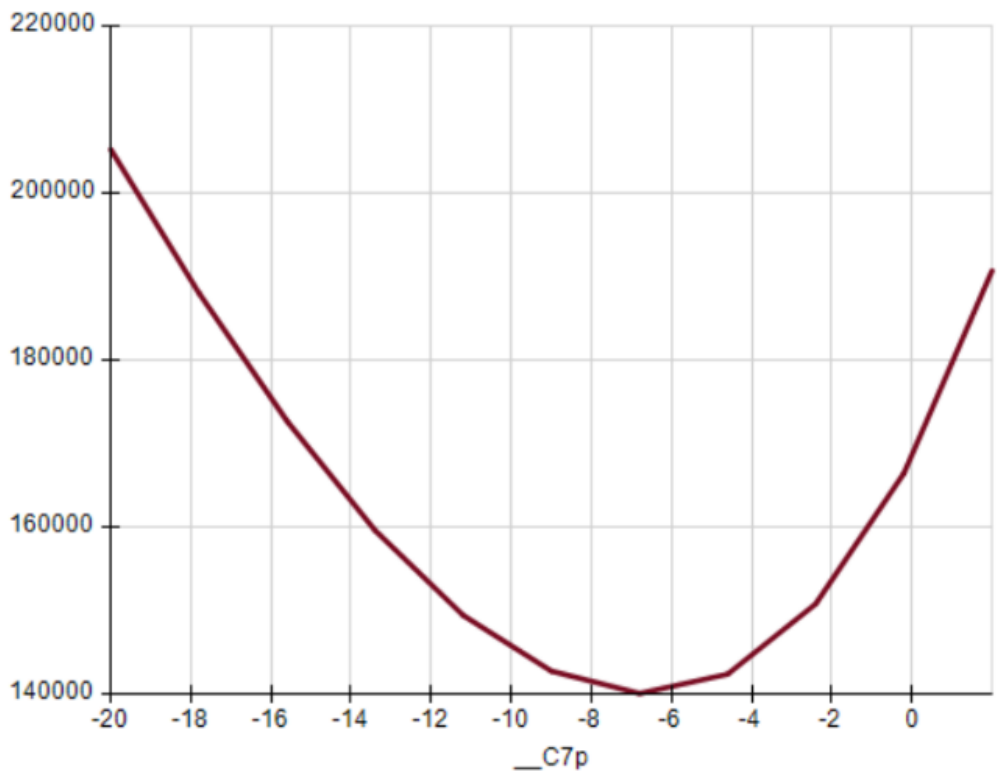
747





748

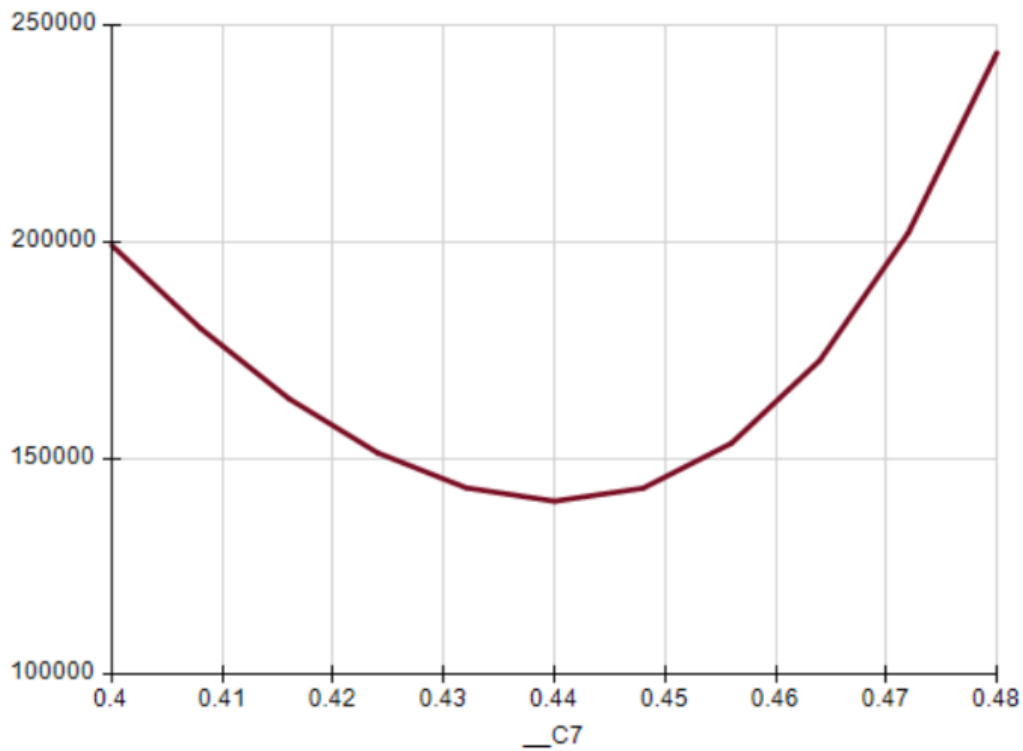
749



150

759

760



769

770

771 Figure S2: Example of sensitivity tests on some regressed parameters. The vertical axis is the  
772 Soptim value. Soptim values < 180,000 define the acceptable range of regressed parameters.

773

774

775 Supplementary references:

776 Jiang, G-R, Li, Y-X, Liu, Y., 2011. Calculation of hydrogen solubility in molten alloys. Trans.  
777 Nonferrous Met. Soc. China 21, 1130-1135.

- 778 Lob, A., Senk, D., Hallstedt, B., 2011. Determination of Hydrogen Solubility in Fe–Mn–C  
779 Melts. *Steel Research Int.* 82, No. 2. DOI: 10.1002/srin.201000262
- 780 Wang, C., Hiramata, J., Nagasaka, T., Ban-Ya, S., 1991. Phase equilibria of liquid Fe–S–C  
781 ternary. *ISIJ International* 11, 1292–1299.
- 782